Descending Reflectivity Cores in Supercell Thunderstorms Observed by Mobile Radars and in a High-Resolution Numerical Simulation

ZACK BYKO, PAUL MARKOWSKI, AND YVETTE RICHARDSON

Department of Meteorology, The Pennsylvania State University, University Park, Pennsylvania

JOSH WURMAN

Center for Severe Weather Research, Boulder, Colorado

EDWIN ADLERMAN

New York, New York

(Manuscript received 18 January 2008, in final form 9 June 2008)

ABSTRACT

This paper is motivated by the recent interest in the ''descending reflectivity cores'' (DRCs) that have been observed in some supercell thunderstorms prior to the development or intensification of low-level rotation. The DRCs of interest descend on the right rear flank of the storms and are small in scale, relative to the main radar echo. They are observed to descend from the echo overhang and, upon reaching low levels, have been found to contribute to the formation or evolution of hook echoes, which are perhaps the most familiar radar characteristic of supercells. Herein, observations of DRCs obtained by a mobile Doppler radar at close range are presented. The data afford higher-resolution views of DRCs and their accompanying radial velocity fields than typically are available from operational radars, although one drawback is that some of the larger-scale perspective is sacrificed (e.g., the origin of the DRC and its possible connection to the reflectivity near the updraft summit are within the cone of silence). It is found that it is difficult to generalize a relationship between the observations of DRCs and the subsequent evolution of the low-level wind field.

The results of a three-dimensional numerical simulation of a supercell thunderstorm also are presented. DRCs are a common development within the simulation despite the use of a simple (warm rain) microphysics parameterization. The simulation allows for an investigation of the aspects of DRCs that cannot be ascertained using single-Doppler radar observations, for example, DRC formation mechanisms, the relationship between DRCs and the three-dimensional wind field, and the thermodynamic fields that accompany DRCs. Three different mechanisms are identified by which DRCs can develop in the model, not all of which are followed by increases in low-level rotation. This finding might account for the aforementioned difficulty in generalizing associations between DRCs and changes in the low-level wind field observed by mobile radar, as well as the fact that prior studies also have produced somewhat mixed results with respect to the potential of DRC detection to aid in the operational forecasting of tornadogenesis.

1. Introduction

Hook echoes and their associated rear-flank downdrafts are known to be associated with the development of low-level rotation in supercell thunderstorms (Markowski 2002). Fujita (1958), in a study of the Champaign, Illinois, tornado of 9 April 1953, carefully documented the formation and evolution of what are believed to be the first hook echoes observed by radar (Stout and Huff 1953). At the time, Fujita hypothesized that the hook echo formed as precipitation was advected around a supercell's rotating updraft.[1] Browning (1965) also examined the evolution of hook echoes and proposed a formation process in accord with Fujita's

Corresponding author address: Dr. Paul Markowski, 503 Walker Bldg., University Park, PA 16802.
E-mail: pmarkowski@psu.edu

[1] Fujita (1965) later proposed that the Magnus force played a role in hook-echo formation.

DOI: 10.1175/2008WAF2222116.1

(see Browning's Fig. 2). The idea that a hook echo forms as hydrometeors from a supercell's main echo region are advected toward the rear of the storm by the rotating updraft seems to have been widely accepted, although Lemon (1976), Forbes (1981), and Rasmussen et al. (2006) have documented hook echoes that form when reflectivity cores descend from aloft to low levels on the rear flank of the storm, initially detached from the main echo at low levels, and subsequently become connected to the main echo to form a hook echo. These observations suggest that hook echoes might not always form from the simple horizontal advection process envisioned by Browning and Fujita. Of course, the evolution of the reflectivity field is never solely a result of the horizontal advection of precipitation anyway, because hydrometeors fall relative to the air; that is, hook-echo formation inescapably involves descending precipitation curtains. Thus, the question is not whether the descent of precipitation cores can contribute to hook-echo formation, but whether a spectrum of hook-echo formation exists, whereby the horizontal advection of precipitation might dominate the evolution of the low-level reflectivity field and formation of some hook echoes at one end of the spectrum [as in the studies by Fujita (1958) and Browning (1965); see also Figs. 1a–d], and hydrometeor fall speeds dominate the evolution of the low-level reflectivity field and hook-echo formation at the other end of the spectrum [as in the cases documented by Rasmussen et al. (2006), to be discussed below; see Figs. 1e–h].

In a study on the interaction of flanking line cells with a supercell, Lemon (1976) found that the formation of a hook echo was associated with the formation of a separate precipitation core on the rear flank of the main echo: ''In the area where cell C1 has merged with the supercell, the hook echo forms and is maintained'' (p. 691; also see his Fig. 3). This observation bears similarity to those of Garrett and Rockney (1962), who noted that small echo dots were occasionally located at the tip of a hook echo. These small echo dots were termed ''asc's,'' or ''annular sections of the cylinder of the storm vortex.'' Garrett and Rockney (1962) believed that these echo dots were a result of radar returns from debris strewn about by a tornado. However, Forbes' (1981) study of the tornadoes that occurred during the Super Outbreak revealed that 62% of the asc's were observed without a tornado. Thus, the asc's likely do not represent debris. Forbes, like Lemon, found that some of the echo dots morphed into the hook echo itself.

Rasmussen et al. (2006) proposed that some of the asc's observed in the literature may be manifestations of a much more important process in hook-echo formation, termed a ''descending reflectivity core,'' or DRC (Figs. 1e–h). They described a DRC as a ''blob'' of enhanced radar reflectivity that descends from the rear of the echo overhang (Browning 1964; Marwitz 1972; Lemon 1982) at the rear of the weak-echo region (Chisholm 1973; Lemon 1977). Rasmussen et al. required that the following criteria be met for a descending reflectivity appendage to be classified as a DRC: the descending echo must be pendant from the echo cap above the weak-echo region (a qualification that they believed ensures the DRC is not a discrete cell of its own, although it will be shown in section 3 that this criterion may not guarantee that DRC formation is independent of neighboring updrafts), the DRC reflectivity must exceed the minimum reflectivity following the path of greatest reflectivity from the DRC reflectivity maximum to the supercell echo core by at least 4 dB, and it must be located in the rear-right quadrant of the supercell (see Rasmussen et al.'s Fig. 3). Weather Surveillance Radar-1988 Doppler (WSR-88D) observations of DRCs indicate that they are accompanied by enhanced rear-to-front (typically westerly) flow when they reach the surface, perhaps a result of vertical advection of westerly momentum from aloft to the ground (Rasmussen et al. 2006). Such a perturbation in the low-level wind would be associated with a couplet of counterrotating vortices. Rasmussen et al. hypothesized that the cyclonic member of the DRC-induced vorticity couplet can be a precursor to tornadogenesis.

In a companion study, Kennedy et al. (2007a) examined a larger sample of DRCs observed in 64 isolated

→

FIG. 1. Comparison of the formation of a pair of hook echoes on (a)–(d) 12 Jun 2005 and (e)–(h) 23 May 2002, as observed in reflectivity fields (dBZ_e) obtained by the Lubbock, TX (KLBB), WSR-88D and the NCAR S-band, dual-polarimetric (S-Pol) radars at the 0.5°-elevation angle. Times in UTC are displayed at the top right of each panel. In the 12 Jun 2005 case [(a)–(d)], a hook echo emerges from the main echo core in time in a manner suggestive of the horizontal advection of hydrometeors playing a dominant role in the formation of the hook echo, similar to what was proposed by Fujita (1958) and Browning (1965). In the 23 May 2002 case [(e)–(h)], a reflectivity maximum first appears to the south of the main echo and detached from the main echo, and this maximum subsequently becomes attached to the main echo to form a hook echo, suggesting that the hook-echo formation was dominated by precipitation descending from aloft. These reflectivity maxima that descend from aloft and may contribute to hook-echo formation and/or evolution have been termed descending reflectivity cores (DRCs) by Rasmussen et al. (2006).

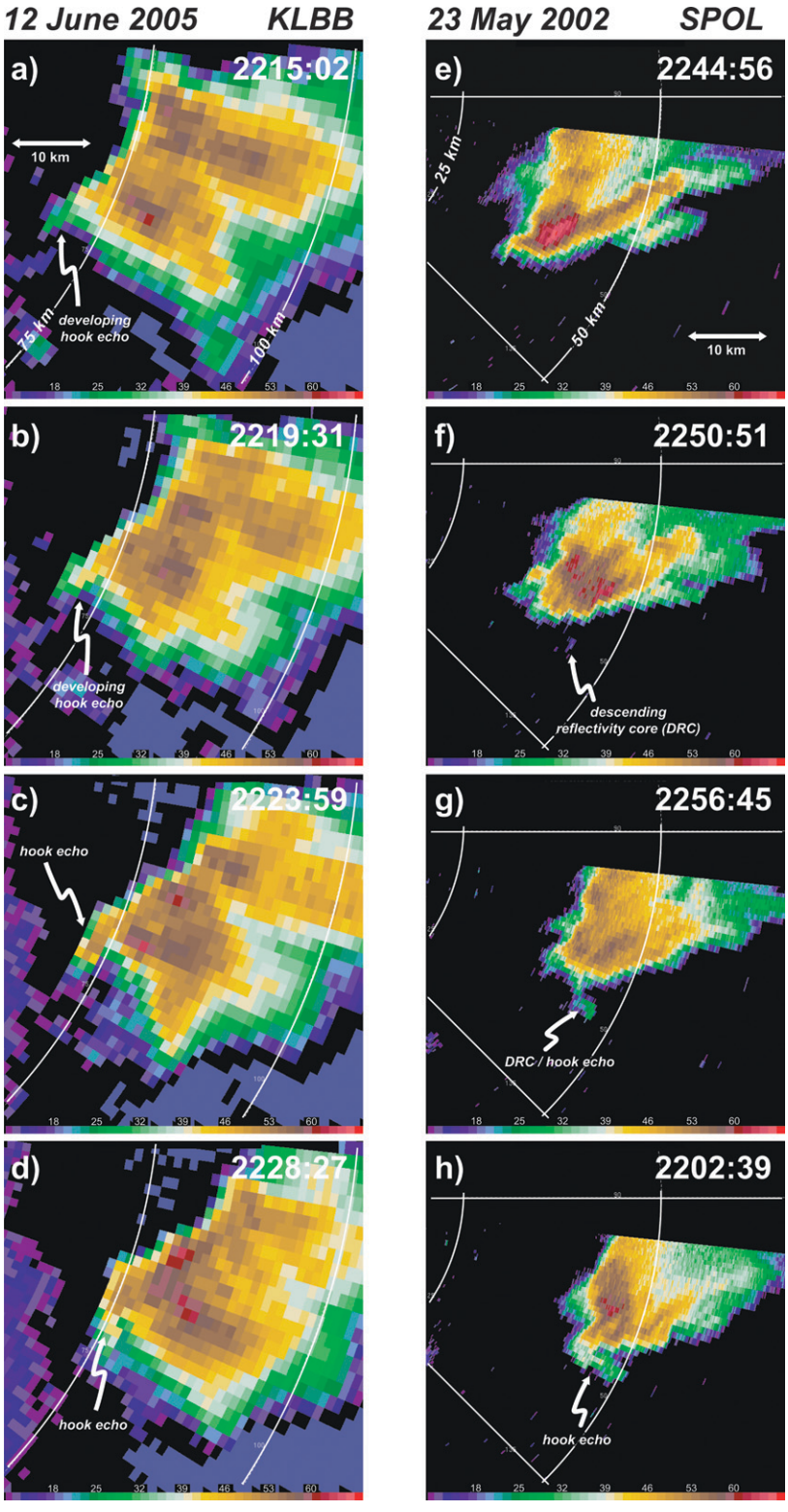
12 June 2005 KLBB
23 May 2002 SPOL
a) 2215:02
10 km
75 km
developing hook echo
100 km
b) 2219:31
developing hook echo
c) 2223:59
hook echo
d) 2228:27
hook echo
e) 2244:56
25 km
50 km
10 km
f) 2250:51
descending reflectivity core (DRC)
g) 2256:45
DRC / hook echo
h) 2202:39
hook echo
18 25 32 39 46 53 60

supercells using WSR-88D data. Of these, 39 (60%) produced at least one DRC, with 19 out of 39 producing multiple DRCs. Kennedy et al. found that 30% (41%) of the DRCs appeared within tornadic supercells on the lowest elevation scan of the radar within the period beginning 10 (30) min prior to tornadogenesis and ending 5 (15) min after tornadogenesis. Kennedy et al. argued that the presence of a DRC may be a better indicator of tornado likelihood than the hook echo, which when used alone, is not a strong tornado–no-tornado discriminator (Forbes 1981; Markowski et al. 2002). Kennedy et al. (2007b) also provided what is believed to be the first visual documentation of DRCs in an isolated tornadic supercell on 6 June 2005.

The purpose of this study is to document DRCs that have been observed by mobile, truck-borne radars [the Doppler on Wheels (DOW) radars (DOW2 and DOW3); Wurman et al. 1997; Wurman 2001] and in a high-resolution numerical simulation [horizontal grid spacing of 105 m; Adlerman (2003)]. One question that arises from the Lemon (1976), Forbes (1981), Rasmussen et al. (2006), and Kennedy et al. (2007a) studies is the degree to which observations of DRCs and hook-echo formation are sensitive to the space and time resolutions of the radar. The radar data available in past studies are somewhat coarse by today's research standards. For example, in the Rasmussen et al. (2006) study, the average distance between the DRCs and the nearest radar was 100 km, and the temporal resolution of the WSR-88D data was 5–6 min. Assuming that a mobile radar typically is deployed much closer to a storm than a fixed radar, the DOW radar data herein provide somewhat finer spatial resolution than has been available in past studies, with typical azimuthal and range resolutions of 25–100 m. The temporal resolution of the DOW data also tends to be better as well, with volumes typically being collected in 1–2 min. The spatial and temporal resolutions of these observations will allow us to confirm the existence of DRCs, putting to rest any questions about their existence stemming from the limitations of WSR-88D resolution, and to better document the relationship between DRCs and the low-level single-Doppler radial velocity field. Moreover, an examination of the numerical simulation in which DRCs were observed will allow us to investigate aspects of DRCs that cannot be ascertained using single-Doppler radar observations (or even dual-Doppler observations, at least not with ease), for example, DRC formation mechanism(s), the relationship between DRCs and the three-dimensional wind field, and the thermodynamic fields that accompany DRCs.

Section 2 presents DOW observations of DRCs. Section 3 documents DRCs within a numerically simulated supercell thunderstorm. Section 4 contains a summary and closing remarks.

TABLE 1. Summary of objective analysis parameters used for the five DOW cases. The range of the DRC from the DOW, the depth over which observations were obtained at the location of the DRC, horizontal and vertical grid spacing Δ, Barnes smoothing parameter κ, and the radius R_c from a grid point, beyond which there is no data influence (the "cutoff radius"), are tabulated.

Case	Range of DRC from DOW (km)	Vertical extent (km)	Δ (km)	κ (km^2)	R_c (km)
29 May 2001a	22	0.1–3.4	0.15	0.24	1.10
29 May 2001b	7	0.1–2.3	0.10	0.02	0.32
5 Jun 2001	15	0.1–3.5	0.15	0.11	0.74
26 May 2000	17	1.5–5.3	0.15	0.14	0.84
27 May 1997	5	3.0–3.5	0.10	0.01	0.25

2. DRCs observed by the DOW radars

a. Data and analysis techniques

Constant-elevation scans of reflectivity from WSR-88D and DOW data collected in supercells were examined for the existence of a local reflectivity maximum in the rear-flank reflectivity appendage that satisfied the Rasmussen et al. (2006) DRC criteria. The main diagnostic tool for verifying whether or not a reflectivity maximum on a constant-elevation scan was associated with a DRC consisted of three-dimensional isosurface renderings of radar reflectivity. Though there is no objective formula for determining the isosurface that best represents the true spatial extent of a particular DRC, isosurfaces that best elucidate the evolution of each DRC are presented, with viewing angles strategically chosen to expose the important details. Five cases are presented herein (Table 1): 29 May 2001 (two DRCs were observed on this day, referred to as "29 May 2001a" and "29 May 2001b" hereafter), 5 June 2001, 26 May 2000, and 27 May 1997. It is worth noting that we are presenting *every* case of a DOW-observed DRC that we know of; that is, the cases have not been "cherrypicked." DOW DRC observations are rare because the DOWs typically are not scanning supercells early enough or broadly enough. Most DOW observations of DRCs were obtained from failed tornado intercepts, for example, when the road network only permitted relatively long-range (from >10 km) scanning of the storm.

To create three-dimensional reflectivity isosurfaces, plan position indicator (PPI) reflectivity fields were ob-

jectively analyzed to a Cartesian grid via an isotropic Barnes objective analysis scheme (Barnes 1964) using the REORDER software of the National Center for Atmospheric Research (NCAR). Table 1 summarizes the vertical sampling, grid spacing, and objective analysis parameters used for each analysis. The grid spacing and degree of smoothing were influenced by the distance between the radar and the region of interest (i.e., the location of the DRC); the grid spacing and Barnes smoothing parameter (κ) increased as the distance to the region of interest increased (Table 1). Reference frame corrections also were performed by following a reflectivity feature in time to determine a translation velocity, then correcting all data points in a radar volume to their position at a centralized time. Values of κ were determined following the recommendations of Pauley and Wu (1990), where $\kappa = (1.3\Delta)^2$ was used, where Δ was the data spacing at the range of the DRC. This approach was a bit less conservative than the approach typically used in dual-Doppler wind syntheses (e.g., Arnott et al. 2006; Markowski et al. 2006), whereby Δ is based on the coarsest data spacing in the domain. Our main interest was in drawing isosurfaces from gridded reflectivity fields (most isosurface-drawing algorithms require a regular grid of data) that retained as much of the original details as possible in the vicinity of the DRCs, rather than allowing the degree of smoothing to be influenced by the data spacing in regions far removed from the DRCs. It was found that more conservative smoothing choices, which are often recommended for other radar applications (e.g., Trapp and Doswell 2000), frequently smoothed DRCs beyond recognition.

One limitation of using DOW data for this study is that, owing to their relatively close proximity to the storm, at least by WSR-88D standards (as stated above, the data herein were obtained serendipitously while attempting to observe tornadoes and tornadogenesis), only the lowest few kilometers are scanned by the radar (Table 1). Thus, though the space and time resolutions of the DOW data are better than that typically afforded by an operational radar like the WSR-88D, some of the larger-scale perspective is sacrificed; for example, the origin of the DRC and its possible connection to the reflectivity near the storm summit are within the cone of silence. Another possible drawback of the DOW data is attenuation, which is greater at the 3-cm wavelength of the DOWs than at the 10-cm wavelength of a WSR-88D. DRC observations could be adversely affected if a DRC is behind a heavy precipitation core from the vantage point of the DOW. This limitation was not problematic in the present study, however, as the DOWs typically were positioned on the southern or southeastern flanks of the storms. Scanning from this direction typically minimizes the amount of intervening precipitation between the radar and DRC.

b. Cases

1) 29 MAY 2001A

The DOWs intercepted a long-lived supercell in the Texas Panhandle on 29 May 2001. A DRC was observed by the Amarillo, Texas (KAMA), WSR-88D and DOWs during the 2223–2238 UTC period (Figs. 2 and 3); the storm was nontornadic during this particular time period. From 2223 to 2228 UTC, WSR-88D PPI scans reveal a relative maximum in reflectivity near, but detached from, the main echo associated with the storm on low-elevation scans (Figs. 2a and 2b). By 2233 UTC this reflectivity maximum connects with the main supercell echo region (Fig. 2c), and by 2243 UTC, a hook echo is apparent in low-level scans (Fig. 2e). An examination of three-dimensional reflectivity isosurfaces from the WSR-88D at the same times (Figs. 3a–c) confirms the descent of a protuberance of higher reflectivity from the echo overhang very similar to the evolution of reflectivity isosurfaces documented by Rasmussen et al. (2006). A similar evolution is evident in the DOW data, but finer-scale details are evident in the reflectivity field (Figs. 2f–j and 3d–k). For example, by 2243 UTC, the reflectivity associated with the DRC becomes deformed into an extremely narrow (<100 m wide) hook echo (Fig. 2j). Comparisons between the evolution of the DRC as viewed by the WSR-88D versus the DOW radars are complicated by the fact that DOW reflectivities are uncalibrated (e.g., it is difficult to choose reflectivity isosurfaces for comparison).

One observation of interest is the change in azimuthal shear near the ground with the descent of the DRC. An examination of azimuthal shear at 0.2 km AGL using DOW3 data shows no clear trend in the azimuthal shear from 2223 UTC (the time the DRC is first evident in low-elevation scans) through 2234 UTC (Figs. 2k–m). It is not until 2238 UTC (15 min after the DRC reaches the surface) that the DOW3 data show a considerable increase in the near-ground cyclonic azimuthal shear [exceeding $\sim 0.01\ s^{-1}$; the increase in rotation also was observed visually by one of the authors (YR)], which coincides with a westerly surge of outflow (Fig. 2n). We cannot assign cause and effect to the appearance of the outflow surge and the increase in azimuthal wind shear. Furthermore, the outflow surge seems somewhat far removed from the DRC (the lead-

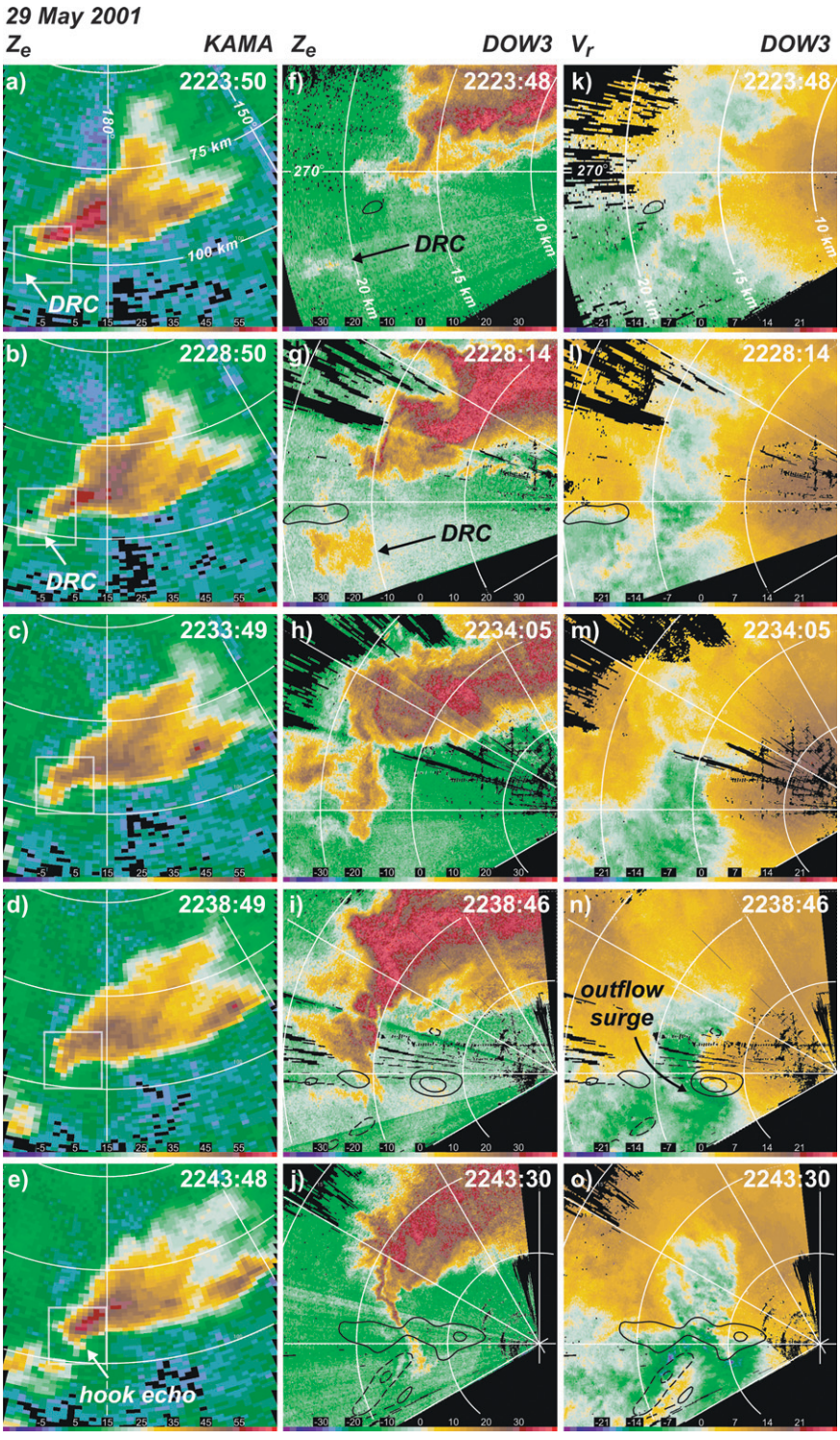

FIG. 2. (a)–(e) Equivalent radar reflectivity factor (dBZ_e) observed by the KAMA WSR-88D at an elevation angle of 0.5° from 2223:50 to 2243:48 UTC 29 May 2001. (f)–(j) Equivalent radar reflectivity factor (dBZ_e) observed by DOW3 at an elevation angle of 1.5° from 2223:48 to 2243:30 UTC 29 May 2001. The reflectivity is uncalibrated. (k)–(o) Radial velocity (m s^{-1}) observed by DOW3 at an elevation angle of 1.5° from 2223:48 to 2243:30 UTC 29 May 2001. In (f)–(o), contours of objectively analyzed azimuthal shear at 200 m are overlaid (0.005 s^{-1} contour interval, negative contours are dashed, the zero contour is suppressed). The region shown in (f)–(o) is the region enclosed by a white box in (a)–(e).

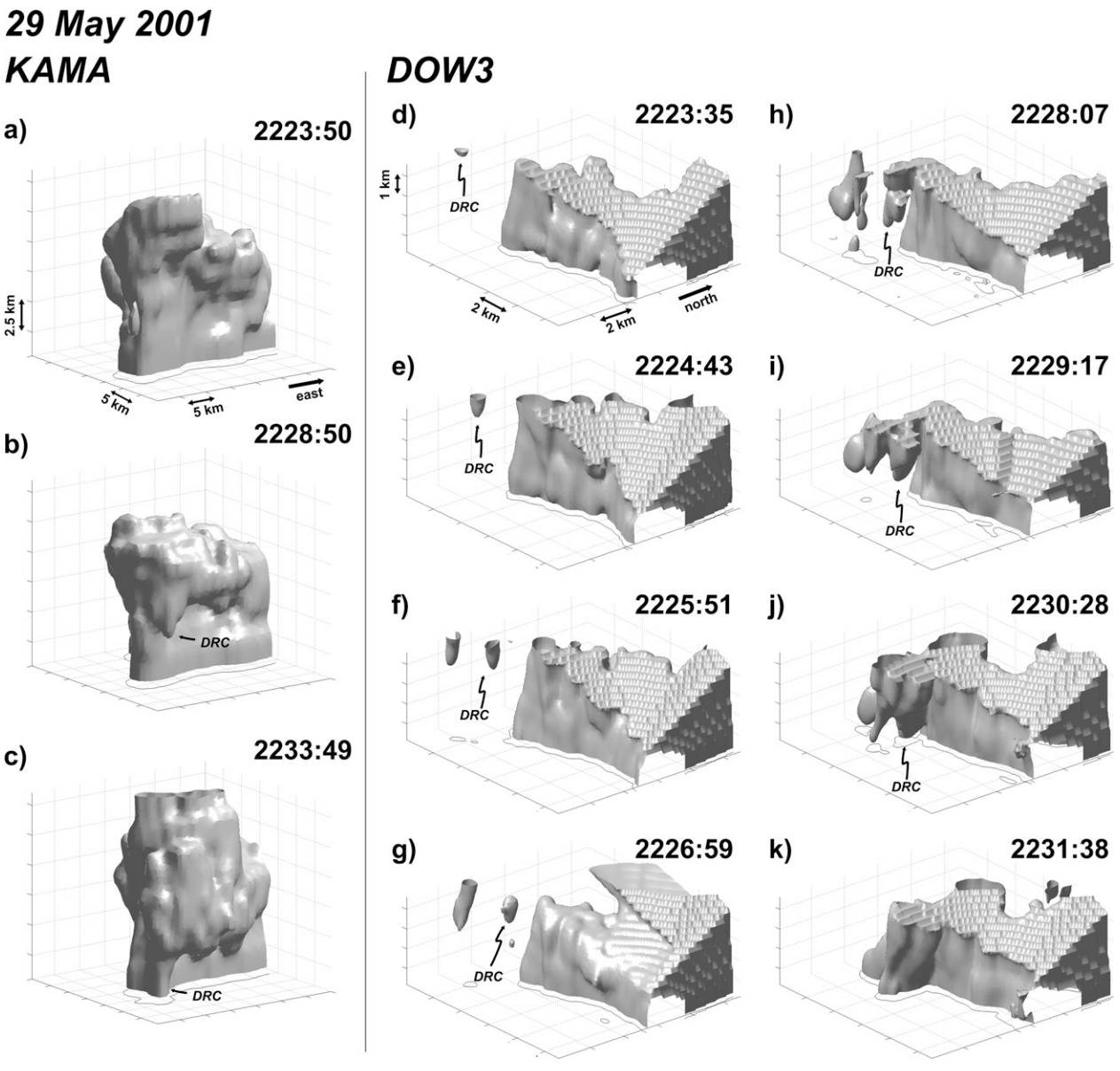

FIG. 3. (a)–(c) Objective analyses of the 32-dBZ_e isosurface as observed by the KAMA WSR-88D from 2223:50 to 2233:49 UTC 29 May 2001. The contour displayed at the bottom of the domain is the 27-dBZ_e reflectivity contour. The view is from the southwest. (d)–(k) Objective analyses of the 8-dBZ_e isosurface as observed by DOW3 from 2223:35 to 2231:38 UTC 29 May 2001. The contour displayed at the bottom of the domain is the 3-dBZ_e reflectivity contour. DOW3 reflectivity values are uncalibrated; thus, comparisons to (a)–(c) should be made cautiously. The view is from the southeast.

ing edge of the outflow surge is ~4 km east-southeast of the southern tip of the hook echo) to be simply the result of enhanced latent chilling (cf. Figs. 2i and 2n).

The formation of the hook echo is similar to the case documented by Lemon (1976), in that the DRC initially appears as though it is a new convective cell southwest of the main cell. The DRC first appears on the lowest DOW scan 5 km southwest of the main echo, and then appears to overtake the main echo and merge with it, in a manner very similar to that observed by Lemon in the case he documented. Given Lemon's conclusion (see section 1), the hook echo in the present case also perhaps formed when a flanking-line updraft merged with the main cell echo region and deposited hydrometeors in the rear-flank echo appendage, causing a DRC to form. A similar explanation to account for some DRC observations was proposed by Rasmussen et al. (2006). The possible role that flanking-line updrafts might play in DRC formation will be revisited in section 3. A sum-

TABLE 2. Summary of the DOW observations of DRCs documented herein.

Case	Summary
29 May 2001a	DRC possibly originated within a flanking-line updraft; westerly (rear to front) low-level outflow increased after the DRC reached the surface, but it was ~15 min later and somewhat spatially distant from the DRC; low-level rotation intensified in conjunction with the outflow surge
29 May 2001b	Pair of DRCs observed 5 min apart; significant low-level azimuthal shear present prior to the DRC reaching the surface weakens following the arrival of the DRCs; region of enhanced westerly outflow is present prior to the detection of the DRCs
5 Jun 2001	DRC likely a result of processes associated with updraft–mesocyclone cycling; arrival of DRC at the surface was followed by an increase in cyclonic azimuthal wind shear along the gust front, although cyclonic shear was present well before the DRC developed; westerly outflow was already well established in the region where the DRC reached the ground before its arrival
26 May 2000	Obvious DRC detected, but origin unknown and changes in low-level winds uncertain owing to limited vertical coverage of data
27 May 1997	Possibly a DRC look-alike; volumetric data unavailable, but no suggestion of the reflectivity maximum originating from higher altitudes (e.g., the sudden appearance of reflectivity values locally larger than any other reflectivity values at the same elevation angle)

mary of the DOW observations in this case and the other cases appears in Table 2.

2) 29 MAY 2001B

Approximately 80 min after the DOWs observed the DRC documented in the previous section, they observed the formation of a distinct, but relatively small, hook echo via another DRC (the supercell also was nontornadic at this time). Prior to 2345 UTC, no hook echo is evident in the DOW data, but in the ensuing minutes, a narrow hook echo forms (Fig. 4d). Inspection of a series of PPI scans of reflectivity data strongly suggests that the hook echo did not form as a result of horizontal advection of hydrometeors from the main radar echo of the storm; that is, a progressive lengthening of a reflectivity appendage was not observed. Instead, reflectivity intensifies simultaneously along the entire length of the hook echo as it develops between 2345 and 2353 UTC (Figs. 4d and 4e). A second DRC is detected at 2356 UTC (Fig. 4f), by which time the hook echo consists of two small-scale bowing reflectivity segments. Both DRCs are prominent in isosurface analyses (Figs. 5d–k).

No DRCs are detected by the KAMA WSR-88D in the 2348–2353 UTC period (Figs. 4a and 4b), and only the slightest hint of a small hook echo and DRC are evident at 2358 UTC (Fig. 4c). DRCs are not resolved in the isosurface analyses during the same time period (Figs. 5a–c). In addition to the long range from the KAMA WSR-88D (90–95 km), the DRCs are relatively small in horizontal scale (~1 km or less) compared to those documented in prior WSR-88D studies (Rasmussen et al. 2006; Kennedy et al. 2007a). (The WSR-88D beamwidth at this range is ~1.5 km.) It is likely for these reasons that the DRCs escaped detection in the WSR-88D data, even though the WSR-88D reflectivity data do otherwise suggest supercell characteristics (e.g., elongated reflectivity core, weak-echo notch on the inflow side of the storm, etc.).

The relationship between the DRCs and the radial velocity fields observed by DOW3 has some significant differences from the relationship reported by the Rasmussen et al. (2006) study. At 2348 UTC, the time at which the hook echo first becomes evident on the lowest elevation scans (Fig. 4d) and higher reflectivities in the DRC are beginning to descend toward the surface (Fig. 5e), a pair of westerly momentum (outflow) ''surges'' are already obvious in the radial velocity data (Fig. 4g); that is, the outflow surges *precede* the arrival of the significant reflectivity at the surface within the DRC, which does not occur until 2353 UTC (Fig. 4h), rather than occurring in conjunction with or after the arrival of the DRC at the surface (Rasmussen et al. 2006). Both outflow surges are straddled by regions of cyclonic and anticyclonic azimuthal shear, consistent with a vertical vorticity couplet straddling the regions of enhanced westerly momentum. The more intense (and easternmost) outflow surge evident at 2348 UTC extends more than 5 km east of the hook echo; given the small scale and weak reflectivity within the hook echo at this time (Fig. 4d), it is difficult to attribute this outflow surge to latent chilling within the DRC. This outflow surge is collocated with a roughly 2 km × 5 km swath of enhanced reflectivity (cf. Figs. 4d and 4g), but this reflectivity region is very likely blowing dust, as opposed to being reflectivity associated with the DRC. The enhanced reflectivity in this region is a maximum at the lowest elevation angle and is not apparent above 400 m. Blowing dust also was reported by the DOW operators at this time. Close inspection of the reflectivity and radial velocity fields at 2348 UTC also reveals that the weaker (westernmost) of the two outflow

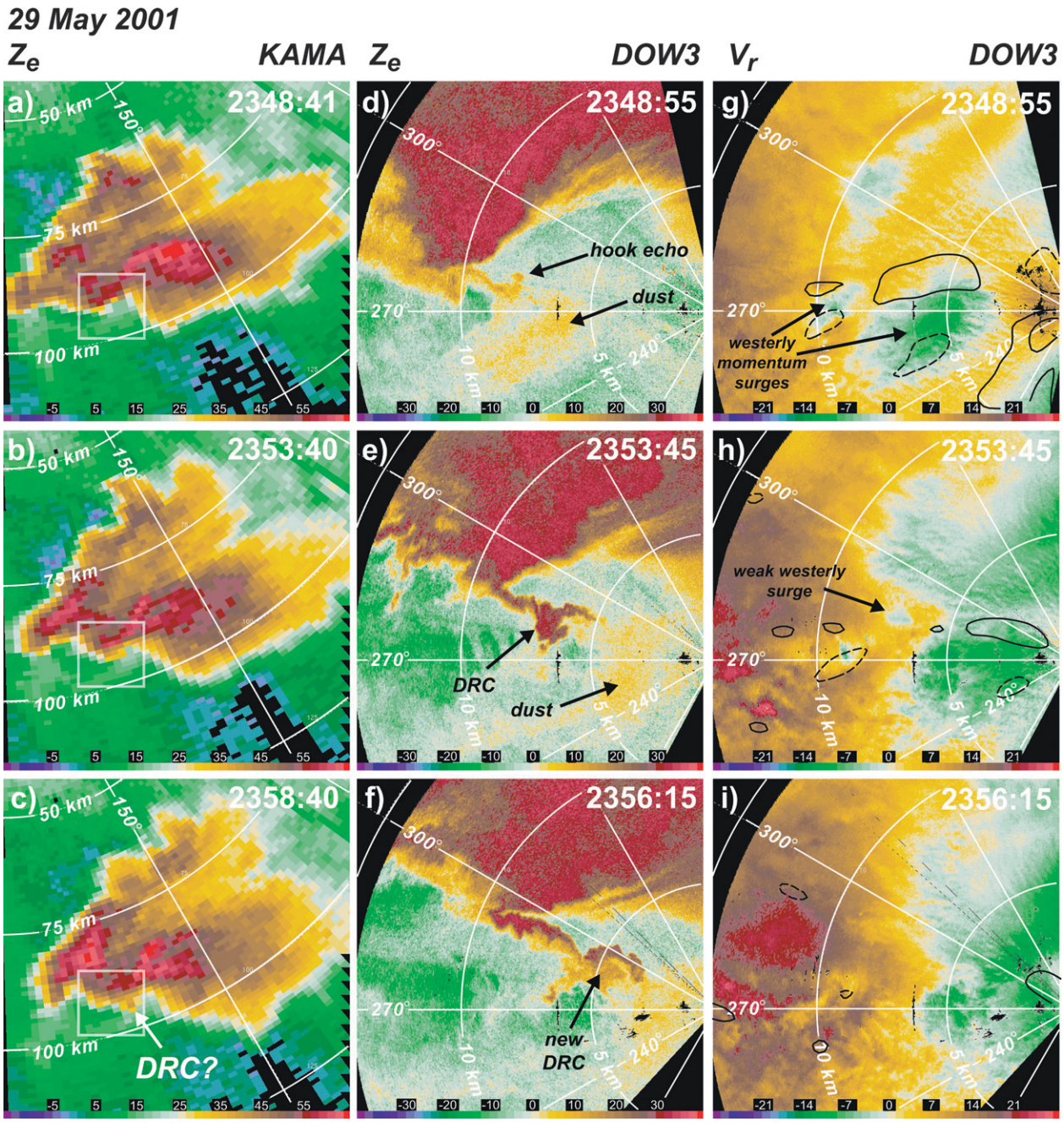

FIG. 4. (a)–(c) Equivalent radar reflectivity factor (dBZ_e) observed by the KAMA WSR-88D at an elevation angle of 0.5° from 2348:41 to 2358:40 UTC 29 May 2001. (d)–(f) Equivalent radar reflectivity factor (dBZ_e) observed by DOW3 at an elevation angle of 1.5° from 2348:55 to 2356:15 UTC 29 May 2001. The reflectivity is uncalibrated. (g)–(i) Radial velocity (m s^{-1}) observed by DOW3 at an elevation angle of 1.5° from 2348:48 to 2356:09 UTC 29 May 2001. In (g)–(i), contours of objectively analyzed azimuthal shear at 200 m are overlaid (0.005 s^{-1} contour interval, negative contours are dashed, the zero contour is suppressed). The region shown in (d)–(i) is the region enclosed by a white box in (a)–(c).

surges is actually located decidedly west of (behind) the hook echo, rather than within it (cf. Figs. 4d and 4g). In summary, the outflow surges evident at 2348 UTC do not appear to be *an effect of the* DRC.

As the reflectivity at low levels within the DRC intensifies from 2348 to 2353 UTC (Fig. 4e), another outflow surge is observed in the immediate vicinity of the DRC (Fig. 4h), but it is small in scale (its area is

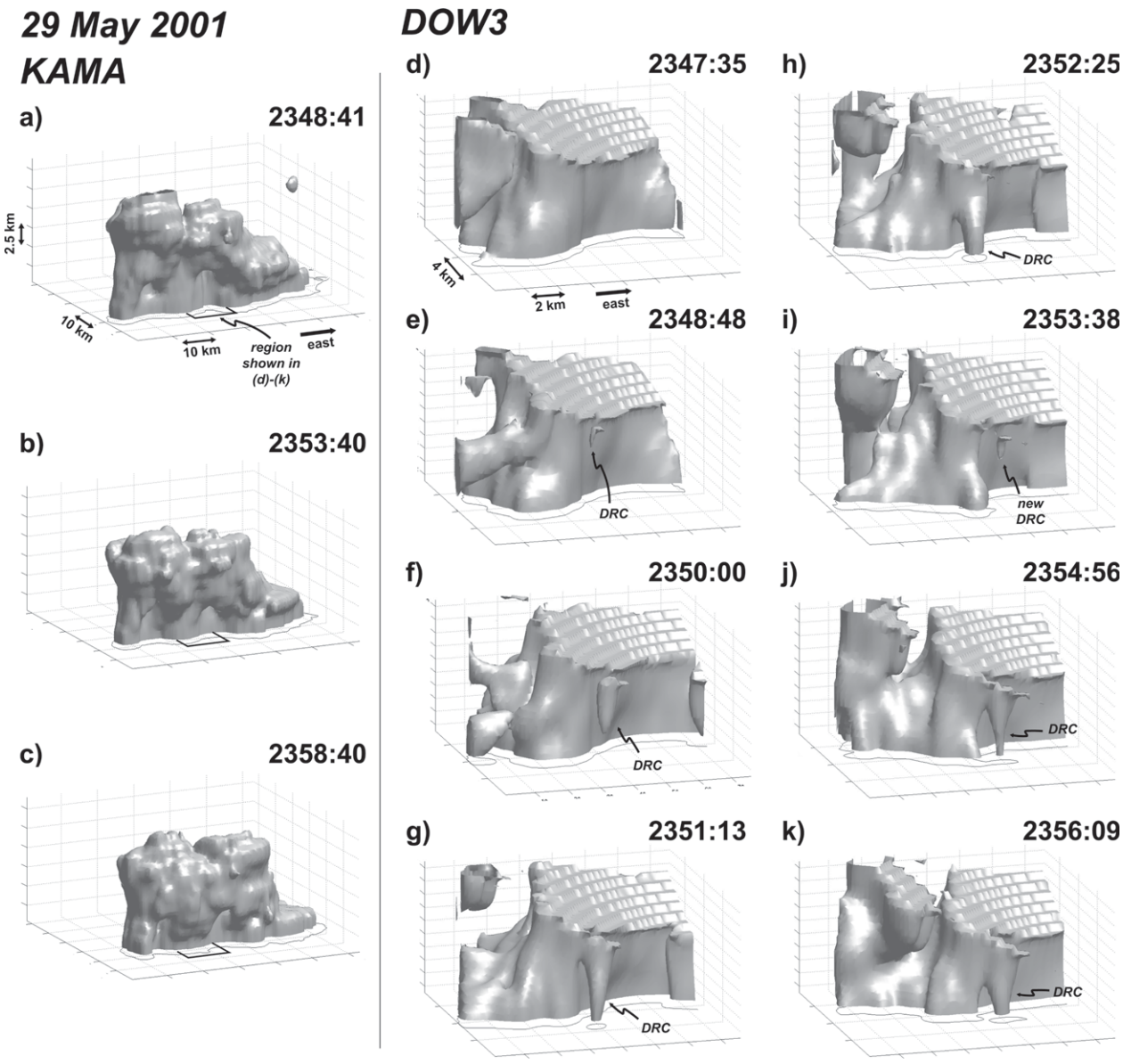

FIG. 5. (a)–(c) Objective analyses of the 40-dBZ_e isosurface as observed by the KAMA WSR-88D from 2348:41 to 2358:40 UTC 29 May 2001. The contour displayed at the bottom of the domain is the 35-dBZ_e reflectivity contour. The view is from the southeast. (d)–(k) Objective analyses of the 23-dBZ_e isosurface as observed by DOW3 from 2347:35 to 2356:09 UTC 29 May 2001. The contour displayed at the bottom of the domain is the 20-dBZ_e reflectivity contour. DOW3 reflectivity values are uncalibrated; thus, comparisons to (a)–(c) should be made cautiously. The view is from the southwest.

<1 km^2), weak [the inbound (westerly) radial velocities in the vicinity of the DRC at low levels are weaker than those within the aforementioned, non-DRC-associated outflow surges observed at 2348 UTC (Fig. 4g)], and not associated with a significant increase in either cyclonic or anticyclonic azimuthal shear on either of its flanks as has been observed by Rasmussen et al. (2006). No significant azimuthal shear or outflow accelerations are evident in the second DRC either, observed at 2356 UTC (Figs. 4f and 4i and 5j and 5k).

3) 5 JUNE 2001

The DOWs observed a DRC in a nontornadic supercell in south-central Kansas on 5 June 2001 that appeared to be associated with updraft–mesocyclone cycling (Burgess et al. 1982; Jensen et al. 1983; Adlerman et al. 1999). WSR-88D data were unavailable for this case. At 2130 UTC, DOW3 began scanning a storm with significant low-level rotation accompanied by a hook echo. Between 2142 and 2154 UTC (Fig. 6), the

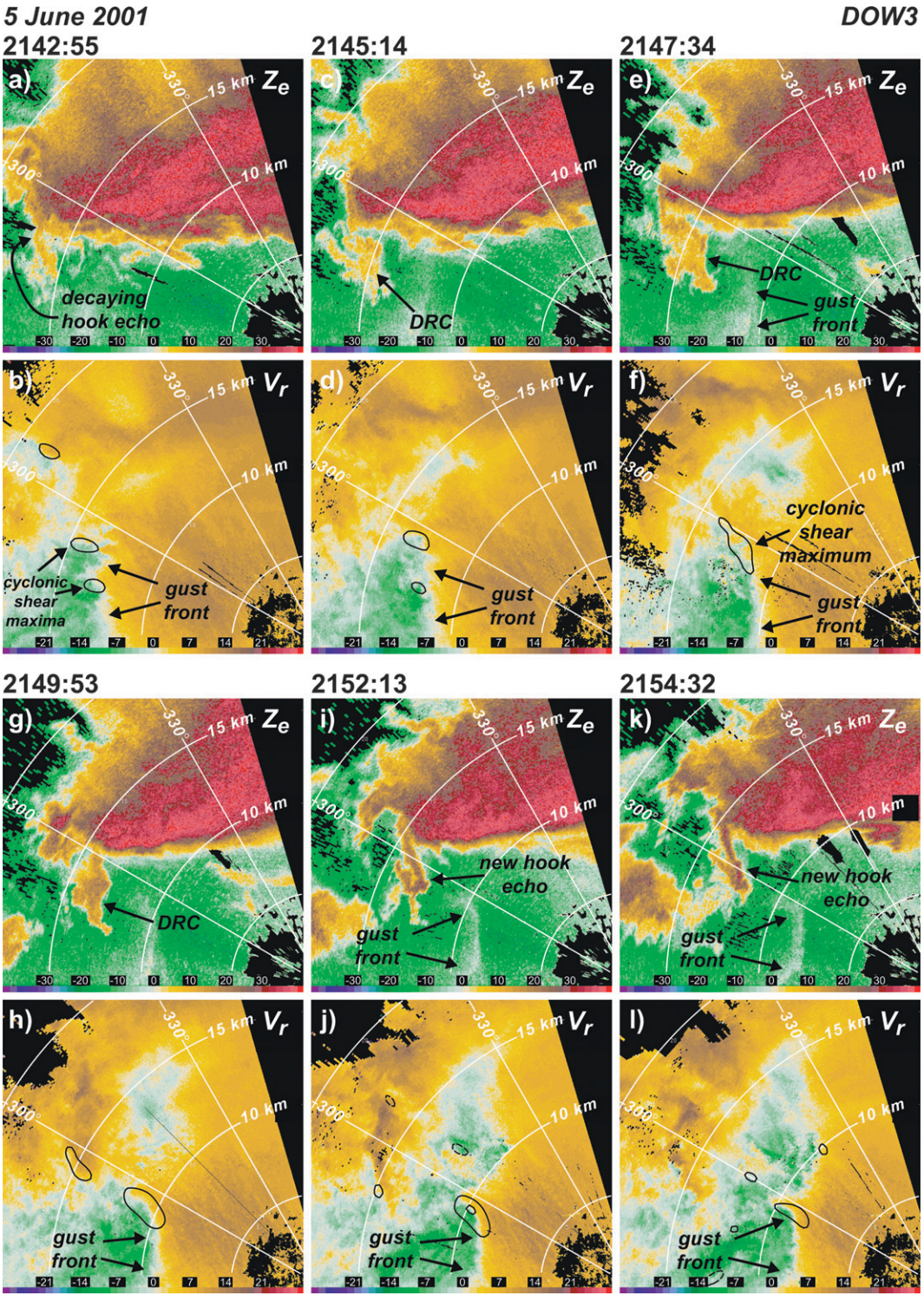

FIG. 6. (a), (c), (e), (g), (i), (k) Equivalent radar reflectivity factor (dBZ_e) and (b), (d), (f), (h), (j), (l) radial velocity (m s^{-1}) observed by DOW3 at an elevation angle of 0.5° from 2142:55 to 2154:32 UTC 5 Jun 2001. The reflectivity is uncalibrated. In the radial velocity panels, contours of objectively analyzed azimuthal shear at 200 m are overlaid (0.005 s^{-1} contour interval, negative contours are dashed, the zero contour is suppressed).

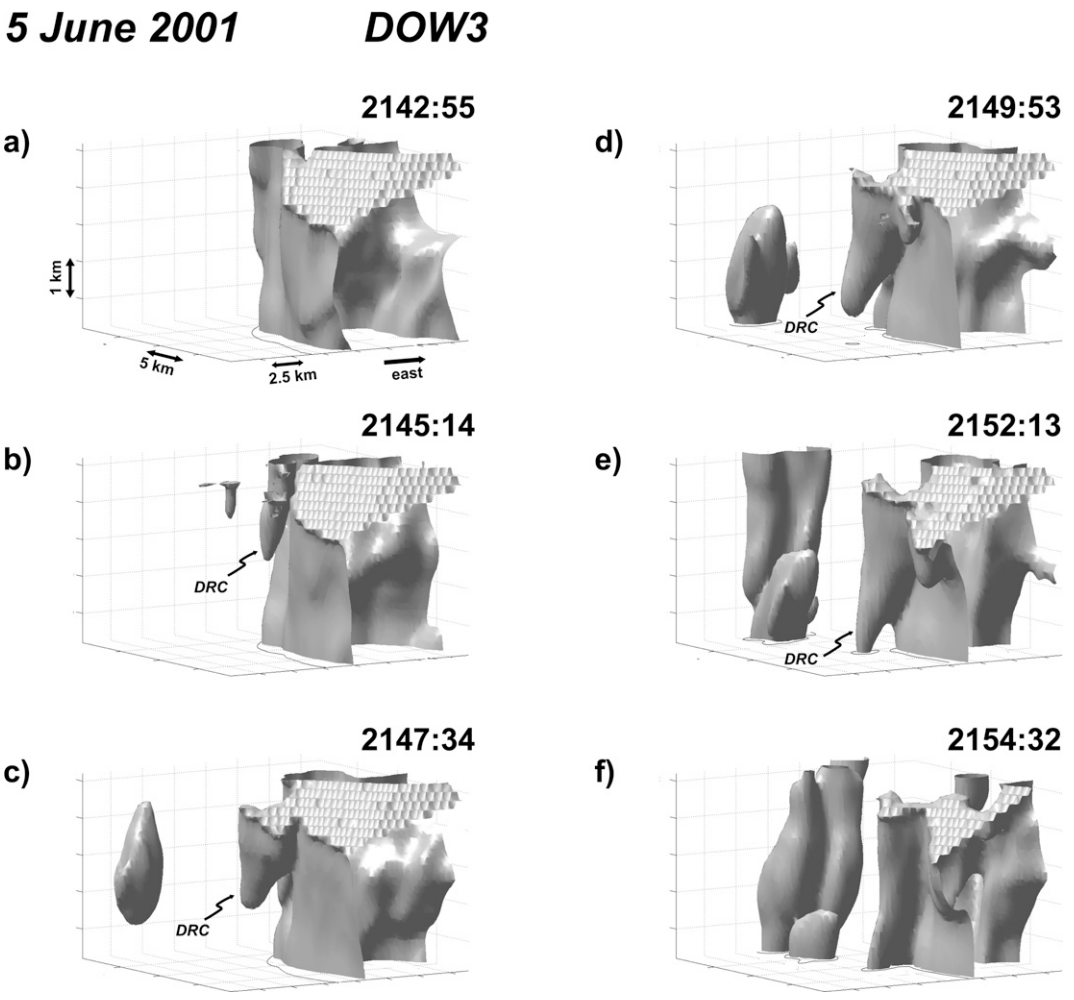

FIG. 7. Objective analyses of the 25-dBZ_e isosurface as observed by DOW3 from 2142:55 to 2154:32 UTC 5 Jun 2001. The contour displayed at the bottom of the domain is the 22-dBZ_e reflectivity contour. The view is from the southeast.

original hook echo decays while a new hook echo forms, as would be expected during storm cycling. Although the reflectivity PPIs in Fig. 6 (particularly panels a, c, and e) might suggest only the translation of a single hook echo, a discrete propagation of the hook echo is evident between 2142:55 (Fig. 6a) and 2145:14 UTC (Fig. 6b) when viewing the reflectivity field at intermediate times (not shown). The isosurface analyses in Fig. 6 also clearly depict the development of a new reflectivity maximum at 2145:14 UTC (Fig. 7b).

Neither PPI scans (Fig. 6) nor isosurface analyses (Fig. 7) suggests a hook-echo evolution dominated by the horizontal advection of hydrometeors from the main echo. Instead, a new hook appears to form as falling hydrometeors enhance reflectivity on the lowest elevation scans. Rasmussen et al.'s (2006) 4-dB local reflectivity maximum criterion is exceeded at 2149 UTC (Fig. 6g). By 2152 UTC, a new hook echo is apparent in the DOW3 reflectivity field (Fig. 6i). Curiously, the 25-dBZ_e isosurface descent rate is only 6 m s^{-1}, which might suggest that the hydrometeors are falling through updraft, the hydrometeors are unusually small, or the hydrometeors are evaporating as they fall.

Prior to the arrival of the DRC at the surface (e.g., 2142 UTC), a pair of cyclonic azimuthal shear maxima are observed along the gust front, east of the dissipating hook echo (Fig. 6b). As the DRC becomes evident on the lowest elevation scans in the 2145–2147 UTC period (Fig. 6c and 6e), the two cyclonic azimuthal shear maxima merge and form a broader area of significant (>0.005 s^{-1}) cyclonic azimuthal shear (Fig. 6f). The region of cyclonic azimuthal shear continues strengthening and attains a maximum at 2152 UTC (Figs. 6h and 6j), at approximately the same time that DOW operators also made visual observations of intensifying low-level rotation (D. Dowell 2001, personal commu-

nication). Anticyclonic azimuthal shear also is observed along the trailing portion of the gust front (e.g., Fig. 6l). In summary, the evolution of the radial velocity field in this case is similar to that documented by Rasmussen et al. (2006) and Kennedy et al. (2007a) in that the arrival of the DRC at low levels was closely followed by an increase in cyclonic azimuthal wind shear along the northern flank of the gust front. One notable difference, however, is that cyclonic wind shear along the gust front long preceded the DRC. Moreover, the DRC was not associated with a surge of low-level westerly momentum; rather, westerly outflow was already well established in the region where the DRC reached the ground before its arrival. It is not known how many of the DRCs studied by Rasmussen et al. (2006) and Kennedy et al. (2007a) were associated with updraft–mesocyclone cycling [A. Kennedy (2006, personal communication) reports that at least a few likely were]. Additional evidence and discussion of DRCs associated with updraft–mesocyclone cycling is presented in section 3.

4) 26 MAY 2000

A DRC was observed by DOW3 in the 2348–2353 UTC period within a supercell thunderstorm that produced a tornado at 0019 UTC (27 May) near Throckmorton, Texas. Although these data serve to further establish the presence of DRCs in mobile radar observations, their utility is limited as DOW3 used a volume coverage pattern containing only angles between 6° and 12°. As a result, data were not obtained in the lowest 2 km of the storm. Furthermore, WSR-88D data are unavailable for this case.

Over the 5 min in which DOW3 scanned the DRC, the reflectivity field morphs from one without a rear-flank echo appendage to one with a local maximum of reflectivity, unattached from the main supercell echo, that with time grows in spatial extent and connects with the main cell echo region to form a hook echo (Fig. 8). As has been found in other cases, the hook-echo evolution is inconsistent with a process dominated by the horizontal advection of hydrometeors from the main echo region. Analysis of the 25-dBZ_e reflectivity isosurface confirms that the hook echo formed from descending precipitation curtains (Fig. 9). Due to the absence of data in the lowest 2 km, however, changes in the low-level wind field associated with the formation of the DRC cannot be assessed. At 2.4 km AGL, a region of cyclonic azimuthal shear develops in the vicinity of the hook echo, although curiously, the maximum shear is positioned slightly west of the hook-echo reflectivity maximum rather than east of it, as one might expect (Fig. 8f). Stronger cyclonic azimuthal shear is present at higher altitudes (3–4 km) in association with a well-developed midlevel mesocyclone, both before and during the descent of the DRC (not shown).

5) 27 MAY 1997

A tornadic supercell that produced a tornado near Glenpool, Oklahoma, at 0011 UTC (27 May; 26 May local time) was intercepted by the DOWs. A detailed account of the intercept and single- and dual-Doppler analyses of tornadogenesis has been presented by Wurman et al. (2007).

At 0001 UTC (27 May), a hook echo is apparent in the reflectivity field of the lowest elevation angles scanned by the Tulsa, Oklahoma (KINX), WSR-88D (Fig. 10a). By 0006 UTC, the hook echo has been replaced by a discrete reflectivity maximum that is detached from the main echo (Fig. 10b). Although the reflectivity maximum has the appearance of a DRC, the presence of a DRC cannot be established by tracking reflectivity isosurfaces (Fig. 11), despite the relatively close range to the WSR-88D (i.e., no *descent* of a reflectivity core is observed). At 0001 UTC the 40-dBZ_e isosurface (a variety of other isosurfaces also were analyzed) forms a vertical ''wall'' at the location of the hook echo that is evident in low-elevation PPI scans (Fig. 11a). At 0006 UTC, the aforementioned 40-dBZ_e isosurface wall thins and develops a break, with a column of high reflectivity remaining to the south of the main echo (Fig. 11b). The reflectivity column also is evident at 0011 UTC (Fig. 11c).

Unfortunately, the DOW data collection is limited to nominally single-elevation angles during this period; thus, no isosurfaces could be constructed. The DOW2 data are limited to the 3.5°–3.9° elevation angles (the data are roughly 150–300 m AGL within a 2-km radius of the center of rotation that becomes the tornado). The DOW3 data have a similar limitation, but the data are at an even higher elevation angle. (We do not attempt to construct reflectivity isosurfaces by combining the reflectivity fields of DOW2 and DOW3 owing to the fact that their reflectivities are calibrated differently; data are only available at nominally two different elevation angles, and even the higher-elevation angle scans of DOW3 do not extend above 1 km AGL.) Nonetheless, the DOW temporal resolution at a single elevation angle in this case is more than 10 times the temporal resolution of the WSR-88D, with a scan being completed every 18 s (every fifth scan is displayed in Figs. 10c–j).

The reflectivity maximum evident in the WSR-88D data at 0006 UTC (Fig. 10b) is clearly evident in the DOW2 data at the same time (Fig. 10e). Notwithstanding the lack of volumetric reflectivity data, there is

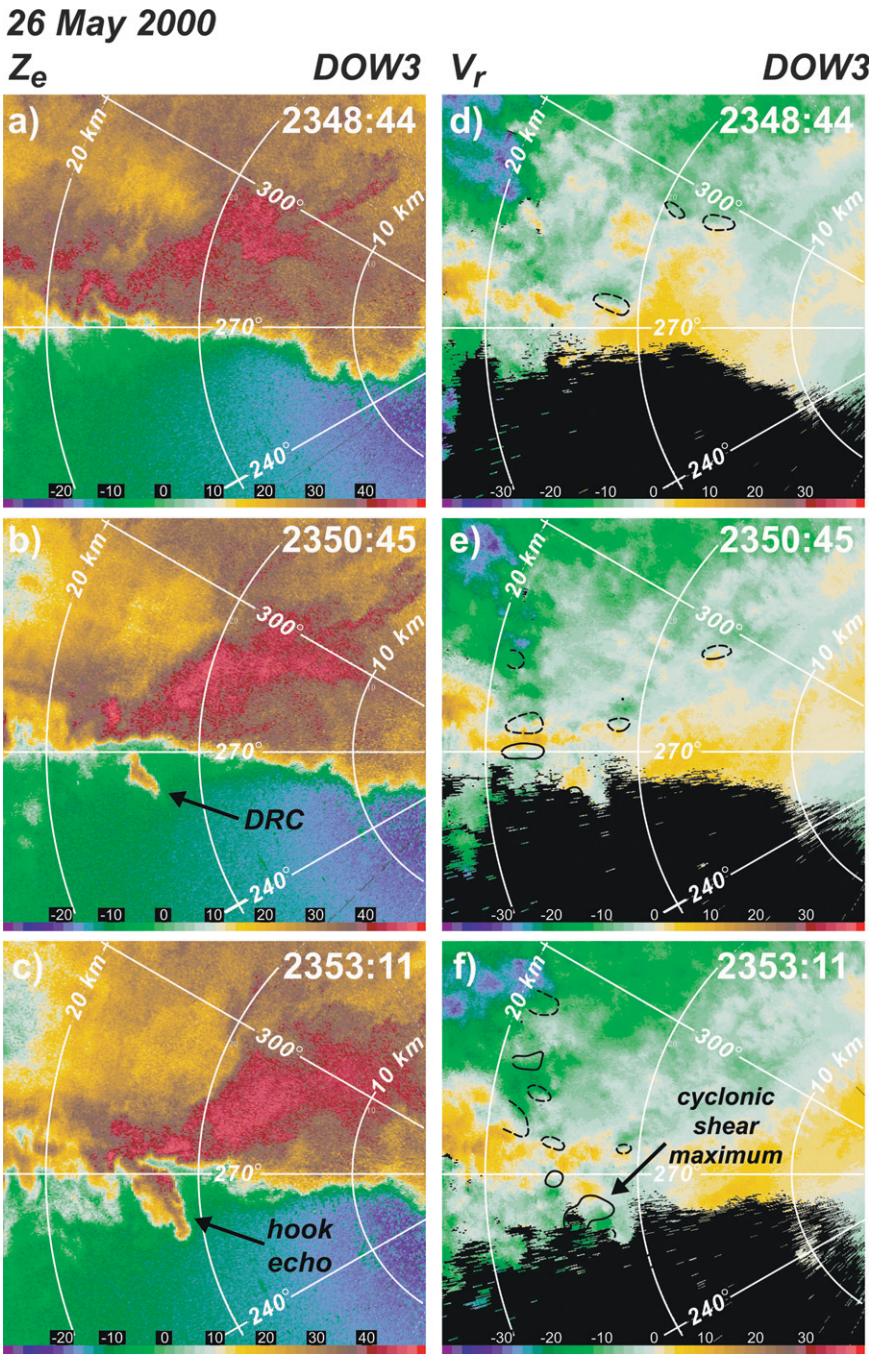

FIG. 8. (a)–(c) Equivalent radar reflectivity factor (dBZ_e) observed by DOW3 at an elevation angle of 6.0° from 2348:44 to 2353:11 UTC 26 May 2000. The height of the beam is approximately 2.2 km at a range of 15 km. The reflectivity is uncalibrated. (d)–(f) Radial velocity (m s^{-1}) observed by DOW3 at an elevation angle of 6.0° from 2348:44 to 2353:11 UTC 26 May 2000. In (d)–(f), contours of objectively analyzed azimuthal shear at 2.4 km are overlaid (0.005 s^{-1} contour interval, negative contours are dashed, the zero contour is suppressed).

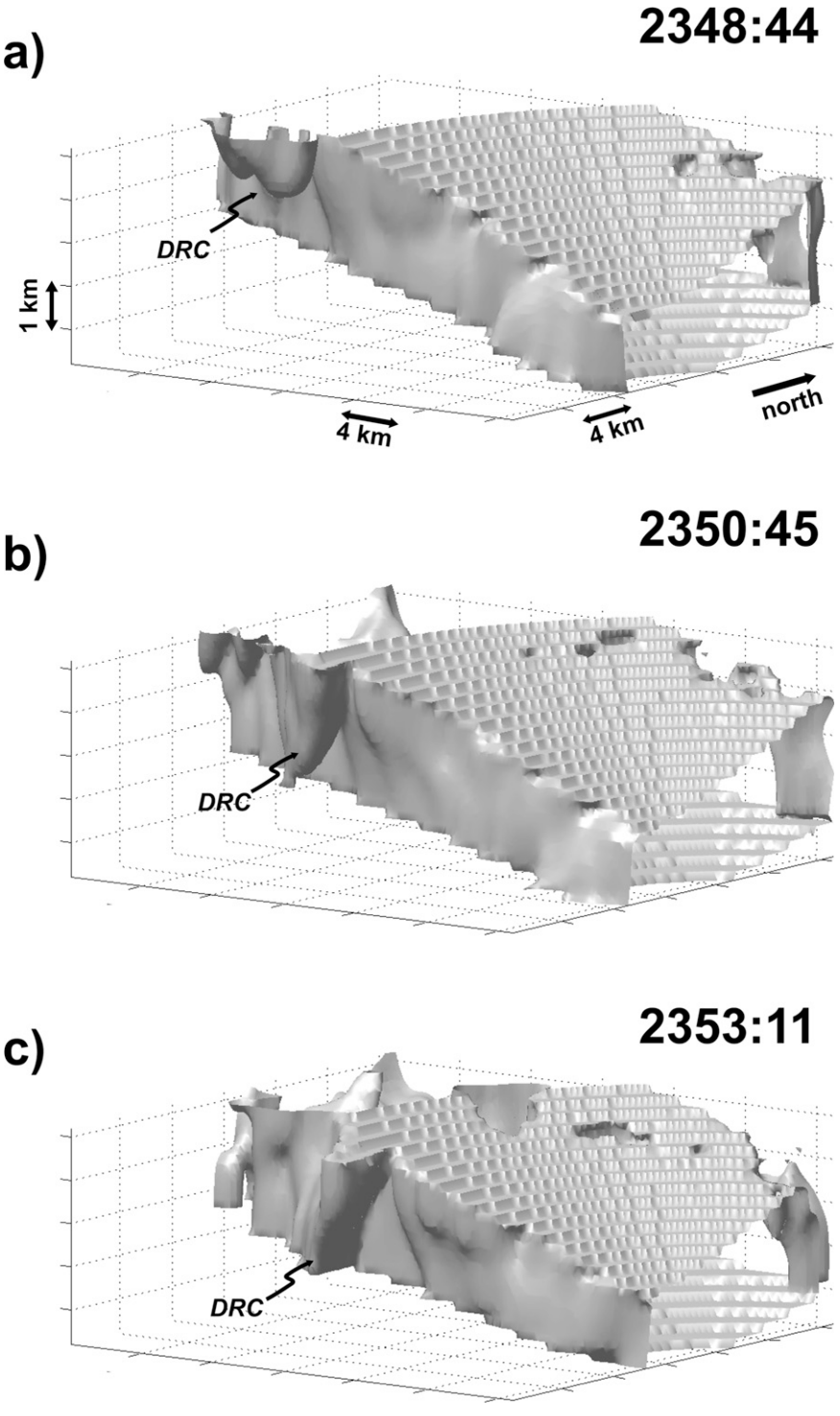

FIG. 9. (a)–(c) Objective analyses of the 25-dBZ_e isosurface as observed by DOW3 from 2348:44 to 2353:11 UTC 26 May 2000. The view is from the southeast.

some suggestion, based on the evolution of this reflectivity maximum in the DOW2 data between 0003 and 0008 UTC (Figs. 10c–f), that the reflectivity maximum evolves predominantly from two-dimensional (horizontal) effects rather than predominantly hydrometeor fall speeds, as is also perhaps suggested by the WSR-88D isosurface evolution (Fig. 11). In all other cases in which DRCs are observed in reflectivity isosurfaces

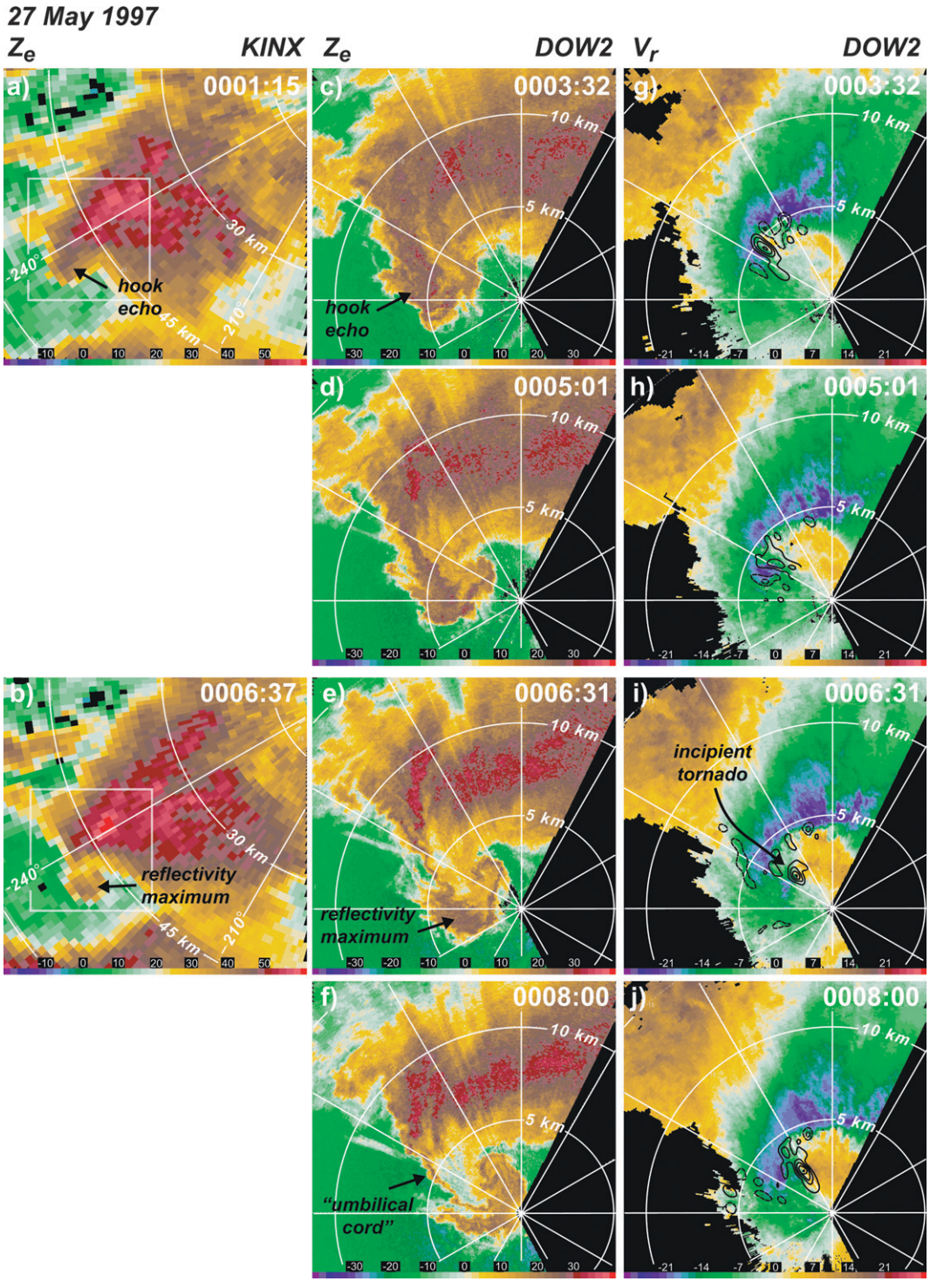

FIG. 10. (a), (b) Equivalent radar reflectivity factor (dBZ_e) observed by the KINX WSR-88D at an elevation angle of 0.5° from 0001:15 to 0006:37 UTC 27 May 1997. (c)–(f) Equivalent radar reflectivity factor (dBZ_e) observed by DOW2 at an elevation angle of 3.5° from 0003:32 to 0008:00 UTC 27 May 1997. The reflectivity is uncalibrated. (g)–(j) Radial velocity (m s^{-1}) observed by DOW2 at an elevation angle of 3.5° from 20003:32 to 0008:00 UTC 27 May 1997. In (g)–(j), contours of objectively analyzed azimuthal shear at 300 m are overlaid (0.010 s^{-1} contour interval, negative contours are dashed, the zero contour is suppressed). The region shown in (c)–(j) is the region enclosed by a white box in (a) and (b).

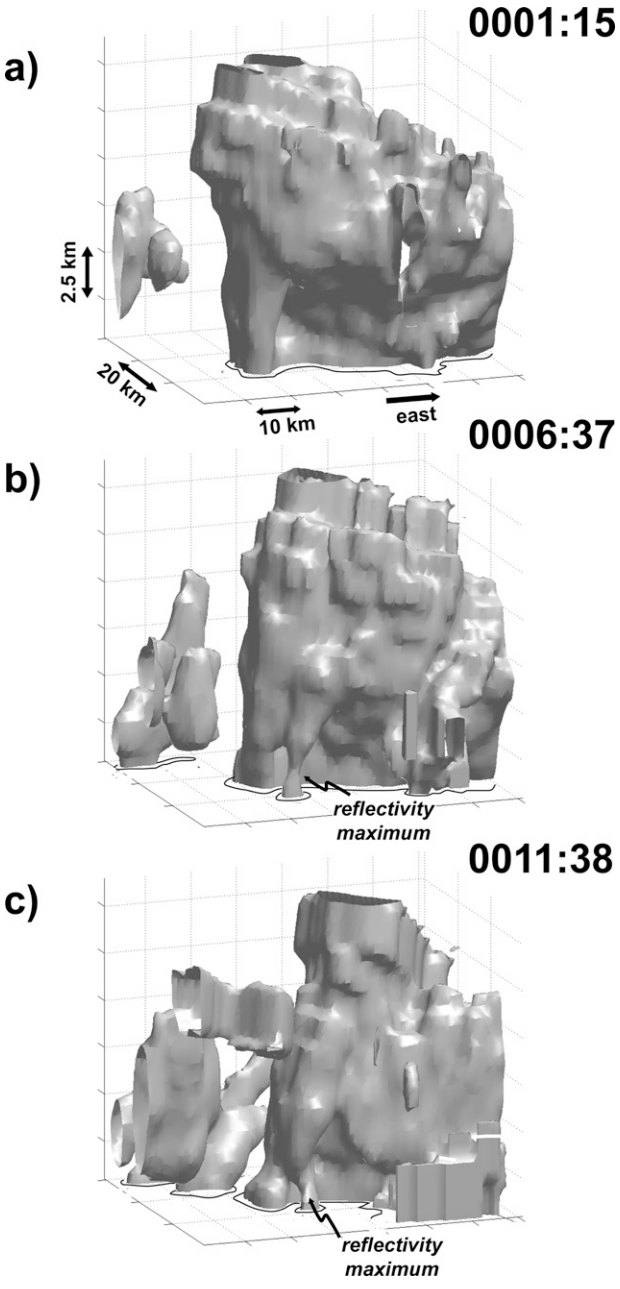

FIG. 11. (a)–(c) Objective analyses of the 40-dBZ_e isosurface as observed by the KINX WSR-88D from 0001:15 to 0011:38 UTC 27 May 1997. The contour displayed at the bottom of the domain is the 37-dBZ_e reflectivity contour. The view is from the southwest.

(constructed either from WSR-88D or DOW data), DOW PPI scans reveal an evolution that is patently inconsistent with horizontal processes dominating the reflectivity field evolution at a single elevation angle; for example, reflectivity values typically appear within the hook, far away from the main echo, that are higher than any other reflectivity between them and the main echo, suggesting they must have come from above (e.g., Figs. 4d–f and 8a–c).

The reflectivity that eventually evolves into a discrete maximum to the south of the main echo is in a region of high winds (radial wind speeds exceed 25 m s^{-1} in parts of the hook echo; Figs. 10g–j) and large horizontal shear and strong rotation (Figs. 10g–j). It is not difficult to imagine that these characteristics of the wind field could have been responsible for the narrowing of the hook echo evident between 0003 and 0008 UTC and transformation of the broad hook echo into an ''umbilical cord'' with a large (several km wide) region of high reflectivity on its end, leading to a DRC look-alike. In other words, we speculate that the discrete reflectivity maximum evident at 0006 UTC in both the WSR-88D data and the DOW data is an *effect of* the wind field rather than a phenomenon that caused the wind field to be as observed. We conjecture that the processes that led to tornadogenesis at 0011 UTC were well under way by 0003 UTC and are what led to the development of a several-kilometer-wide reflectivity maximum by 0006 UTC.

3. DRCs in a numerically simulated supercell

a. Simulation overview

To explore the relationship between DRCs and the three-dimensional wind and thermodynamic fields that accompany DRCs, output from a high-resolution numerical simulation of a supercell thunderstorm (Adlerman 2003) is examined. The simulation is similar to that used by Adlerman et al. (1999) to investigate cyclic mesocyclogenesis, but with finer resolution. The Advanced Regional Prediction System (ARPS) version 4.4 (Xue et al. 2000, 2001, 2003) is used with a two-way nested grid (Skamarock and Klemp 1993). The coarse outer grid encompasses a domain of 70.3 × 70.3 km^2 with a horizontal grid spacing of 525 m and provides boundary conditions for the finer inner grid. The inner grid, which contains the simulated storm and moves along with it, is 22.6 × 22.6 km^2 and has a horizontal grid spacing of 105 m. The 16.7-km-deep vertical domain contains 44 levels, with the vertical grid spacing varying from 70 m at the surface to 700 m at the top of the domain. A fourth-order advection scheme is employed, and the Coriolis force, surface physics, and terrain are all excluded. The Kessler (1969) warm cloud microphysics parameterization is used. This parameterization is known to produce unrealistically cold outflow [see Markowski (2002) and references therein]. It is possible that the dynamical effects of a DRC would be diminished in such a simulation; for example, the low-level flow might be dominated by the cold pool dynam-

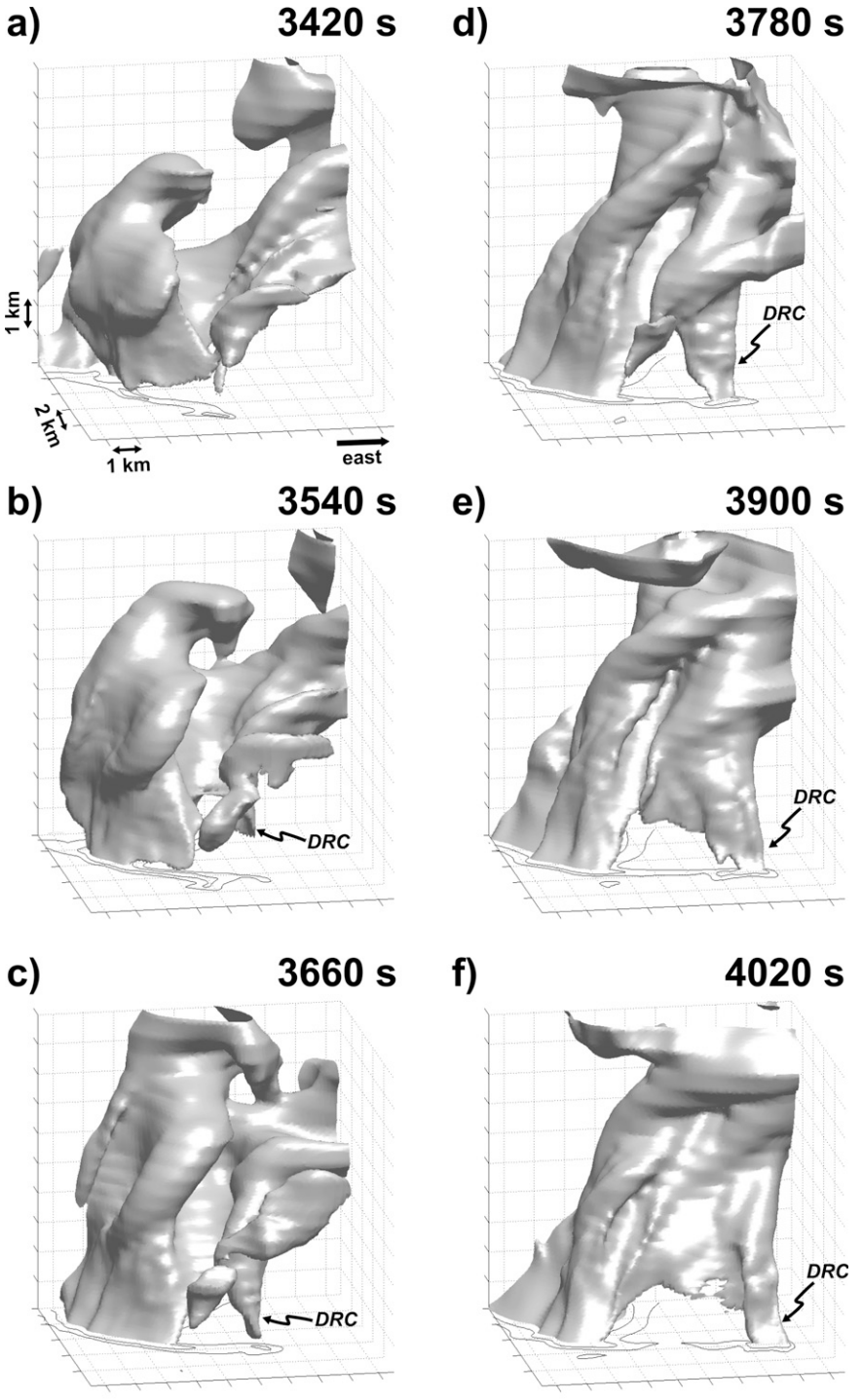

FIG. 12. (a)–(f) Evolution of the 2.5 g kg^{-1} rainwater mixing ratio isosurface in the three-dimensional numerical simulation from 3420 to 4020 s. Only a portion of the domain is shown. The 1 and 2 g kg^{-1} rainwater mixing ratio contours at $z = 35$ m (the lowest model level) also are plotted. The view is from the southwest.

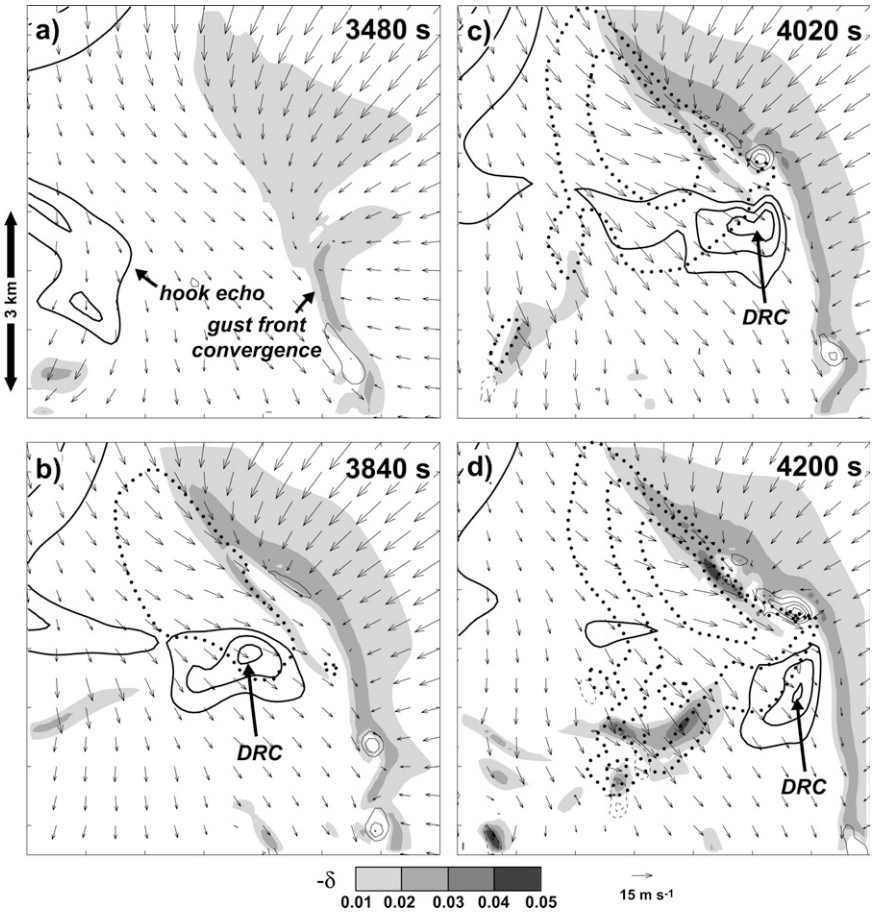

FIG. 13. Zoomed-in view (the location of the domain shown above is indicated in Fig. 14a) of horizontal convergence ($-\delta$; gray shading; see legend), vertical vorticity (contoured at 0.04 s^{-1} intervals; the zero contour is suppressed and dashed contours indicate negative vertical vorticity), rainwater mixing ratio (boldface contours at 1 g kg^{-1} intervals starting at 1 g kg^{-1}), zonal wind (10, 15, and 20 m s^{-1} dotted contours), and horizontal velocity vectors (see legend; vectors are plotted at every fifth grid point) at 35 m (the lowest model level) at (a) 3480, (b) 3840, (c) 4020, and (d) 4200 s, respectively.

ics already in place before the descent of the DRC, and any DRC-related downdraft would be damped and its baroclinity diminished upon penetrating the cold pool. Thus, the relationships between the simulated DRCs and low-level kinematic fields should be viewed with some skepticism. Although these relationships are described in the ensuing subsections, the focus is on DRC formation instead.

The simulation is initialized with a horizontally homogeneous environment defined by a sounding composited from the 20 May 1977 Del City, Oklahoma, supercell case (Ray et al. 1981; Johnson et al. 1987). The environment is characterized by very large convective available potential energy (~4000 J kg^{-1}) and no convective inhibition. The vertical wind profile is very favorable for cyclonically rotating supercells due to the presence of significant wind shear and veering of the shear with height. Convection is initiated by an ellipsoidal thermal bubble. The simulation runs for 5 h, with history files being saved every 30 s beginning at 3300 s. Additional details about the simulation design are provided by Adlerman (2003).

b. Findings

DRCs are found to develop somewhat regularly within the simulation.[2] Three different mechanisms are

[2] Radar reflectivity factor (Z) was computed from the model rainwater field via $z = 17\,300\rho\, q_r^{7/4}$ and $Z = 10\log_{10}z$, where z is the radar reflectivity ($mm^6\ m^{-3}$), ρ is the air density (kg m^{-3}), and q_r is the rainwater mixing ratio (g kg^{-1}), in order to assess whether the rainwater maxima satisfied Rasmussen et al.'s (2006) reflectivity-based DRC criterion.

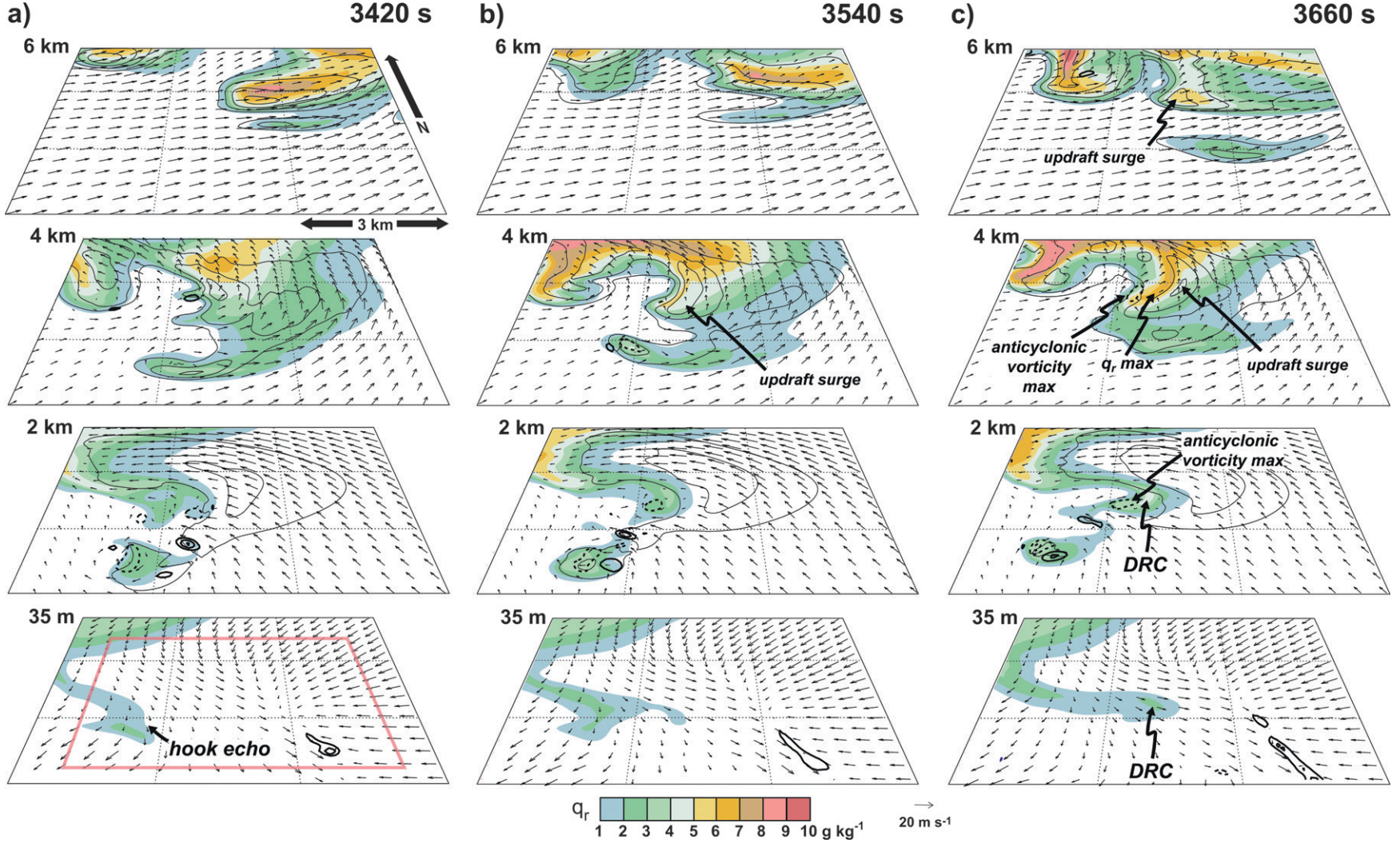

FIG. 14. Rainwater mixing ratio (q_r; color shading—see legend), vertical velocity (black contours of 7, 14, 21, 28, 35, and 42 m s^{-1}; the lowest contour value of 7 m s^{-1} contour very roughly equals the parameterized terminal fall speed of the rainwater maximum in the DRC at $z = 2$ km), vertical vorticity (heavy black contours at 0.04 s^{-1} intervals; the zero contour is suppressed and dashed contours indicate negative vertical vorticity), and horizontal wind vectors (see legend; vectors are plotted at every fifth grid point) at 35 m (the lowest model level) and at 2, 4, and 6 km at (a) 3420, (b) 3540, (c) 3660, (d) 3780, (e) 3900, and (f) 4020 s, respectively. The domain shown in Fig. 13 is outlined in red in (a) (35 m).

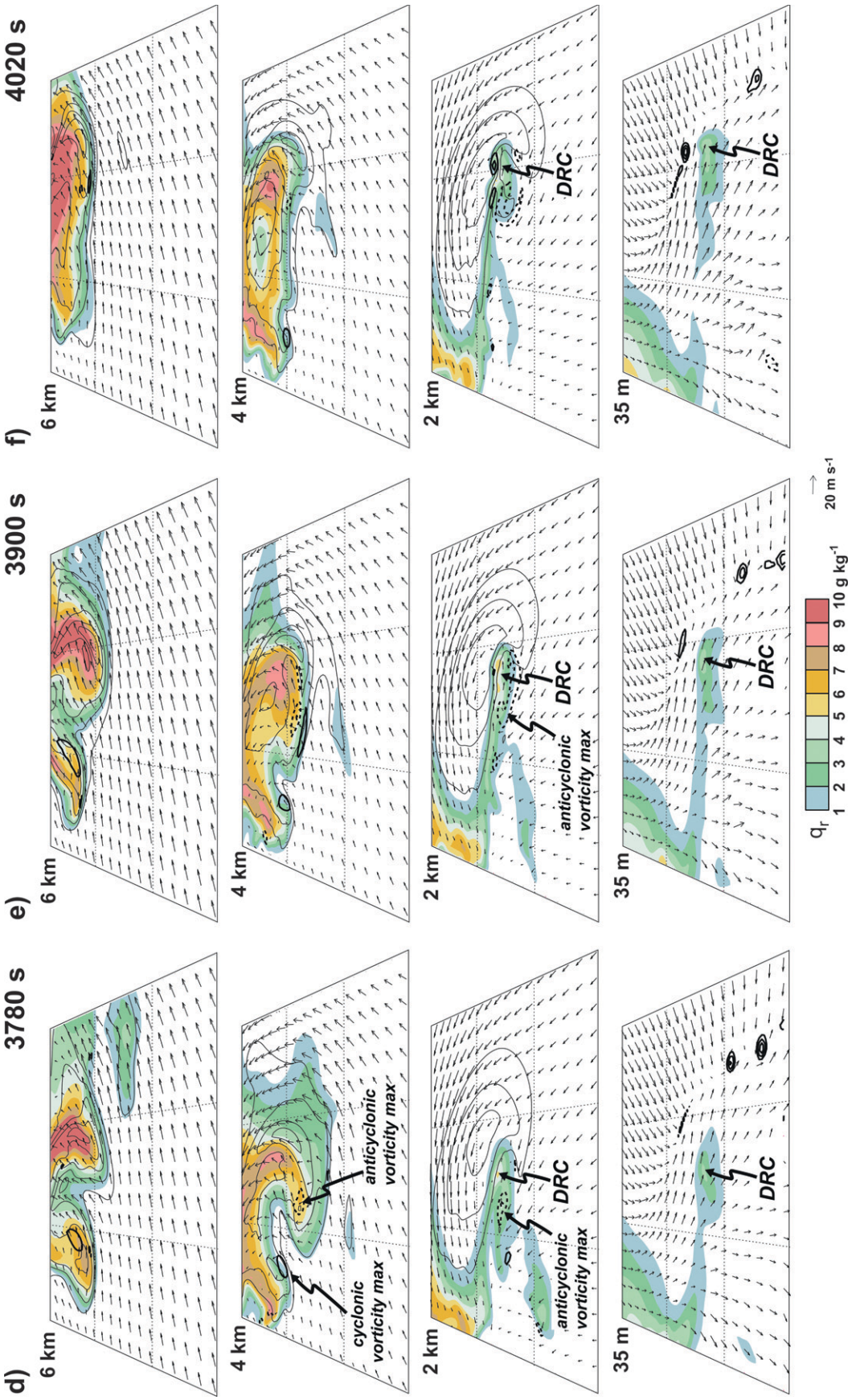

FIG. 14. (*Continued*)

identified by which DRCs developed in the modeled storm. Each of these mechanisms is associated with a distinctly different aspect of the evolution of the storm and its attendant wind field. We do not wish to convey that these are the only three ways by which a DRC might form. It is possible that a larger suite of simulations with a range of microphysics parameterizations would identify additional or different DRC formation mechanisms.

1) DRC formation resulting from stagnation of midlevel flow (type I)

A prominent DRC develops in the simulated supercell at 3420 s and reaches the surface by 3780 s (Figs. 12–15). Shortly after the arrival of the DRC at the surface, a strong cyclonic vorticity maximum (0.17 s^{-1}) develops by 4200 s along the gust front approximately 1 km north of the DRC (Figs. 13b–d). Although the arrival of the DRC at low levels is accompanied by an increase in the low-level rear-to-front flow within the outflow [the westerly wind at 35 m (the lowest model level) increases from <10 to >20 m s^{-1} from 3480 to 4200 s; Fig. 13], similar to the associations between DRCs and outflow surges reported by Rasmussen et al. (2006) and Kennedy et al. (2007a), it is not obvious that the DRC is directly responsible for the increase in westerly momentum in this case for the following reason: the westerly outflow enhancement is centered roughly 3 km to the *northwest* of the DRC (Figs. 13b–d). It is therefore difficult to imagine how the DRC would have directly led to the outflow enhancement. [Also recall in the 29 May 2001b case observed by the DOWs that both an outflow surge and DRC were observed, but that an obvious connection between the two (e.g., the DRC promoting a subsequent westerly acceleration of outflow) was missing.] Regardless of the mechanism responsible for the westerly acceleration within the low-level outflow between 3420 and 4200 s, the outflow surge is associated with an increase in the horizontal convergence along the gust front. The evolution of the vorticity maximum along the gust front resembles the transformation of a vortex sheet into discrete vorticity patches via horizontal shearing instability (Fig. 13). Furthermore, there is no evidence of an anticyclonically rotating counterpart on the south flank (right flank, looking downwind) of the DRC, at least not within 5 km of the DRC (Fig. 13).

The DRC descends on the western flank of the updraft, within cloud, where precipitation fall speeds exceed the updraft speed. Although this limits evaporation within the DRC to the subcloud layer, the DRC still is associated with significant horizontal buoyancy gradients [proportional to gradients in the density potential temperature (Emanuel 1994, p. 161). perturbation fields plotted in Fig. 15] well above cloud base (i.e., as high as 2 km; Figs. 15b and 15c) as a result of hydrometeor loading in the DRC and positive buoyancy in the neighboring updraft. The horizontal vorticity vectors at 1 and 2 km are noticeably perturbed along the periphery of the DRC by its horizontal buoyancy gradients at 3660 and 3900 s compared to 3420 s (Fig. 15), with the vortex lines implied by the vorticity vectors forming loops around the buoyancy minimum associated with the DRC, similar to that envisioned by Straka et al. (2007; their Figs. 5b and 5c). Perhaps surprisingly, however, at $z = 35$ m the DRC has a somewhat limited impact on the buoyancy and horizontal vorticity field (Figs. 15b and 15c), despite the potential for evaporative chilling within the DRC below the cloud base. It seems as though the thermodynamic and wind fields near the ground were dominated by the strong cold pool that was present before the DRC arrived at the ground there. It is possibly for this reason that the location of the DRC was not well correlated with the aforementioned outflow surge. As discussed earlier in this section, the overdevelopment of cold pools is a well-known problem of Kessler microphysics and, therefore, may have prevented the DRC from having a significant dynamical effect of its own.

One of the leading hypotheses for DRC formation broached by Rasmussen et al. (2006, p. 937) was that ''flow stagnation at the rear of the updraft creates a narrow zone where precipitation develops and descends without being swept around the updraft and deposited toward the forward flank.'' As best we can determine, the process by which this DRC develops seems similar to what Rasmussen et al. described (we define this as a type I DRC; Fig. 16). The DRC observed in the model between 3420 and 3780 s forms as a result of a fortuitous superpositioning of the rainwater, vertical velocity, and vertical vorticity fields. Approximately 5 min before the DRC reaches low levels, the updraft begins to intensify (Figs. 14a–d, most evident at 2 and 4 km). This updraft surge leads to an increase in rainwater (via the autoconversion of cloud water to rainwater) at the updraft summit, and this rainwater immediately spills down the western flank of the updraft owing to the combination of updraft tilt (to the west to northwest in the 3420–3540-s period; Figs. 14a and 14b) and the environmental storm-relative winds in the 2–4-km layer (toward the northwest through north; Fig. 14a and 14b). The rainwater accumulates in what we casually refer to as a stagnation zone on the rear side of a broader horseshoe-shaped updraft (in a horizontal cross section), in part because of a couplet of vertical vorticity on the rear side having opposite signs and straddling the

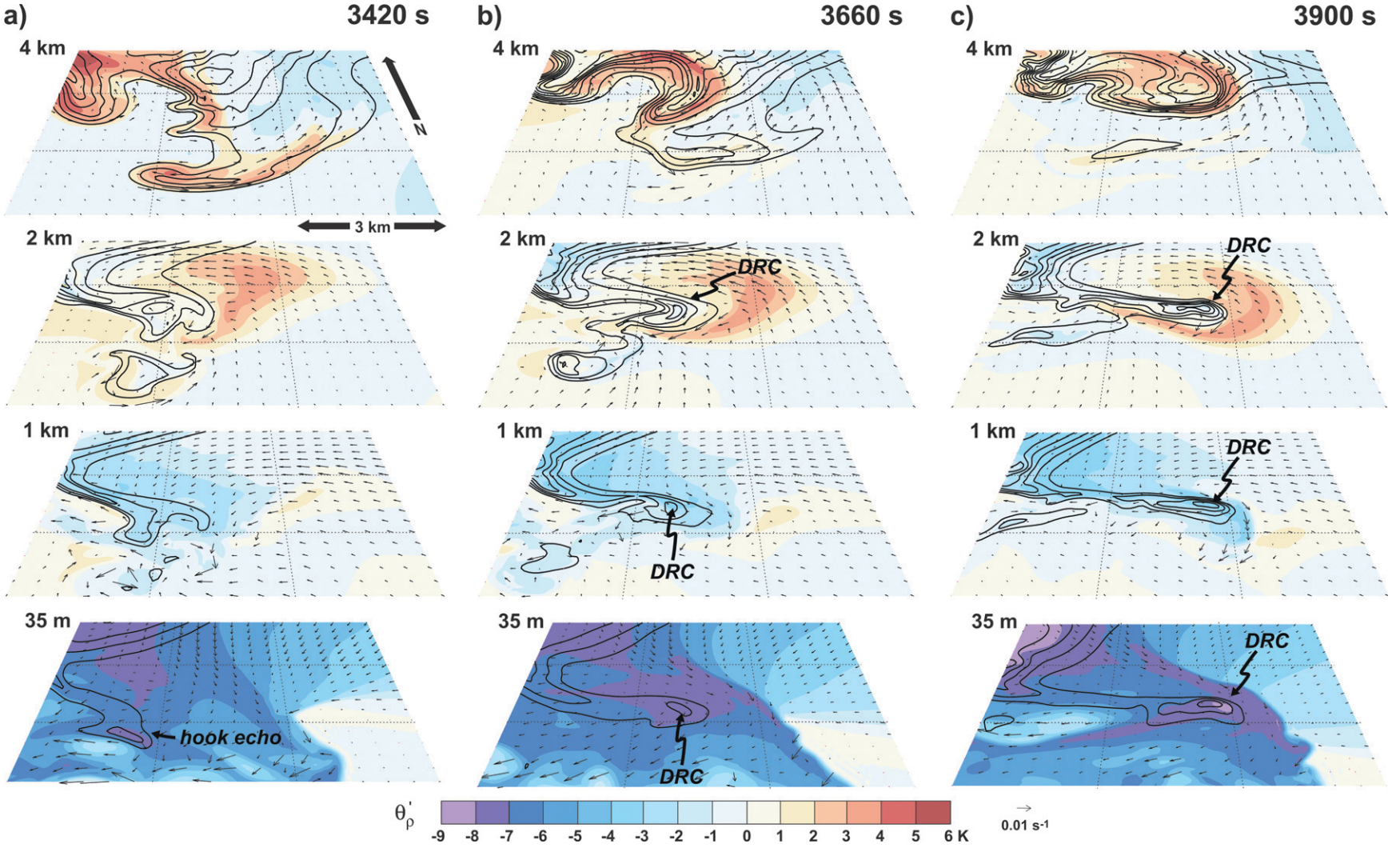

FIG. 15. Density potential temperature perturbations (θ_ρ';*thinsphbox*; *thinsphbox*;color shading—see legend), rainwater mixing ratio (black contours at 1 g kg^{-1} intervals starting at 1 g kg^{-1}), and horizontal vorticity vectors (see legend; vectors are plotted at every fifth grid point) at 35 m (the lowest model level) and at 1, 2, and 4 km at (a) 3420, (b) 3660, and (c) 3900 s, respectively. The horizontal domain shown is identical to that in Fig. 14.

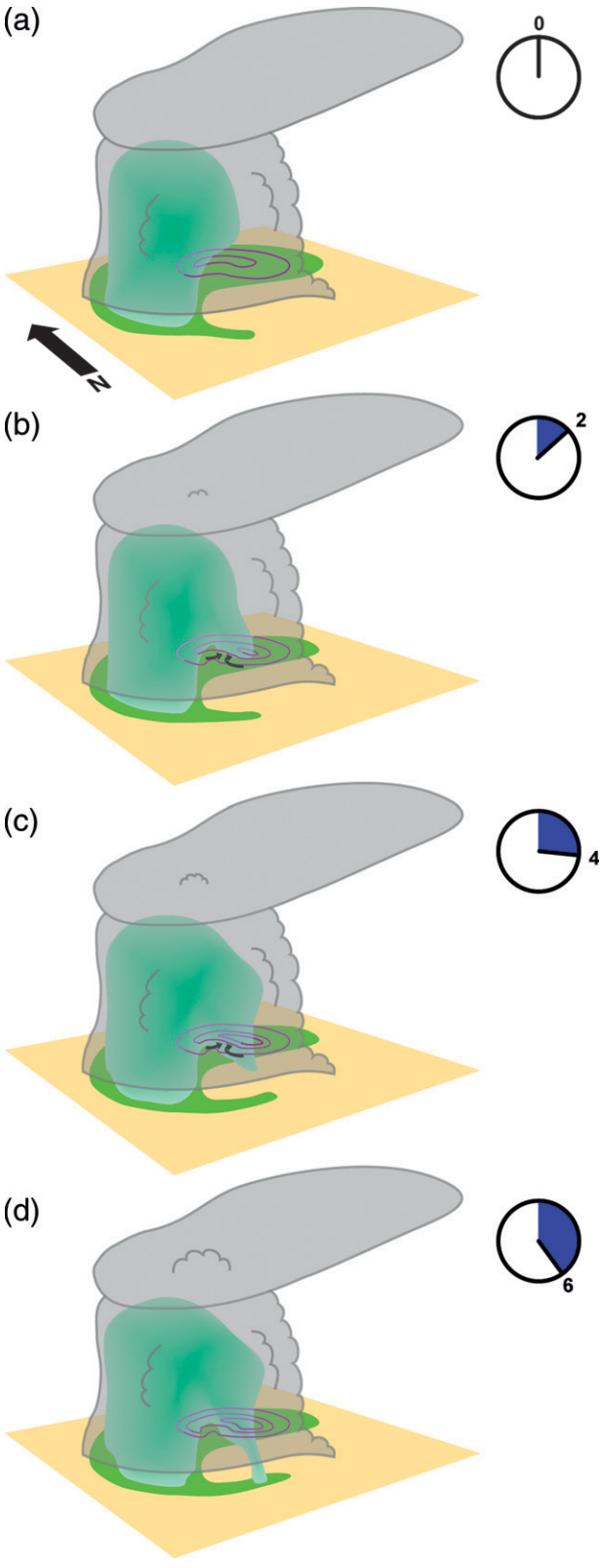

horseshoe (e.g., Fig. 14d, especially at 4 km). The anticyclonic member of the couplet is notably stronger than the cyclonic member, especially at 2 km (Figs. 14c–f); strong anticyclonic vertical vorticity extrema have been documented in similar locations in a number of observed supercells (e.g., Bluestein and Gaddy 2001; Markowski 2008). The rainwater then falls from this stagnation zone once its terminal fall speed, parameterized as a function of the rainwater mixing ratio (Kessler 1969), exceeds the updraft speed (the parameterized terminal fall speed for a rainwater mixing ratio of ~4 g kg^{-1}, which is representative of the maximum rainwater concentration at 2 km in the period from 3540 to 3900 s, is 7 m s^{-1}). The above sequence of events seems rather delicate, and, in fact, a DRC is produced in this fashion only once during the entire 5-h simulation.

Though it seems unlikely that the intensification of the vortex immediately after the DRC arrived at the surface was merely coincidental, the cause-and-effect relationship between the DRC and the intensification of the vortex is beyond the scope of the present study. Our purpose herein is limited to documenting DRCs that have been observed in high-resolution radar observations and in a high-resolution numerical simulation, and, when possible, their attendant kinematic and thermodynamic fields and formation mechanisms. Nonetheless, the most plausible dynamical connections between this DRC and the vortex intensification are via either (i) an increased susceptibility of the gust front to barotropic instability associated with the enhancement of rear-to-front low-level flow that accompanied the arrival of the DRC at the surface (although we again note that the outflow surge was displaced to the northwest of the DRC; thus, cause and effect is not obvious) or (ii) the generation of baroclinic vortex lines within the horizontal buoyancy gradient surrounding the DRC

←

FIG. 16. Conceptual model of a type I DRC. The cloud outline is gray, the dark green isosurface represents larger rainwater concentrations (nominally $q_r > 3$ g kg^{-1}), the rainwater field ($q_r > 0$ g kg^{-1}) at the surface is shaded light green, and vertical velocity contours indicate the midlevel updraft strength. The procession of time is illustrated by the clocks (numerals indicate minutes past the initial time). The evolution is as follows: (a) and (b) an updraft surge occurs and rainwater developing at the summit of the growing updraft begins falling down the western flank of the updraft by the time the summit reaches heights of just 4–6 km (the western flank is favored because of the tilt of the updraft and storm-relative winds in the 2–4-km layer), (c) a couplet of vertical vorticity on the rear side of the updraft promotes the accumulation of rainwater in a ''stagnation zone'' on the western (upshear) flank of the midlevel updraft, and (d) when the rainwater concentration and its attendant fall speeds become sufficiently large, the rainwater maximum descends to the ground as a DRC.

and the subsequent descent and tilting of the vortex lines to produce vertical vorticity, as shown in idealized simulations by Straka et al. (2007).

2) DRC FORMATION RESULTING FROM SUPERCELL CYCLING (TYPE II)

The notion of supercell ''cycling'' originated from observations of tornado families (e.g., Darkow and Roos 1970; Fujita et al. 1970; Fujita 1975; Forbes 1975, 1977). Although early explanations for tornado families included the presence of multiple tornadoes revolving around a single mesocyclone center (Snow and Agee 1975; Agee et al. 1976), the most accepted explanation today is that cyclic tornadogenesis results from the development of a new updraft and mesocyclone following the occlusion of the initial updraft–mesocyclone (Lemon and Doswell 1979; Burgess et al. 1982). Five distinct updraft–mesocyclone ''cycles'' occur in the 5-h numerical simulation. Supercell cycling (i.e., the conclusion of one cycle that coincides with the beginning of the next cycle) typically involves the descent of a new rain curtain on the rear flank of the storm, which becomes a new hook echo. Several of the cycling events in the simulation are associated with DRCs (we define these as type II DRCs), at least as defined by Rasmussen et al. (2006). Below we describe the cycling episode and attendant DRC that occurred in the 5820–6870-s period (Fig. 17).

At 5820 s, a well-defined hook echo is evident, along with a distinct updraft region to the east of the hook echo (Fig. 18a). Over the next few minutes, a new updraft begins to form approximately 3 km south of the center of the original updraft (Figs. 18b and 18c). This new updraft expands northward and strengthens, taking on a classic horseshoe shape (Lemon and Doswell 1979) and becoming the main storm updraft by 6450 s (Fig. 18d). As the new updraft intensifies, the original hook echo dissipates and is replaced by a new hook echo a few kilometers to the east of the original hook echo (Figs. 18e and 18f). The new hook echo has its beginnings as a DRC, and the precipitation responsible for the DRC originates near the summit of the new, intensifying updraft (Figs. 17b and 17c). The DRC is first detectable in isosurface analyses at approximately 6240 s as a downward extension of the main precipitation core along the right-rear flank (Fig. 17c). As the new updraft is intensifying, the precipitation protuberance grows laterally and falls toward the ground. The DRC falls through saturated air along the periphery of, but within, the new updraft. The evolution is summarized in Fig. 19. Whereas the DRC discussed in the previous subsection descended in almost a perfectly vertical manner, this DRC tilts rearward with height (Figs. 17d–f). [Kennedy et al. (2007a) also found examples of DRCs with varying degrees of forward and rearward tilt.] Significant near-ground rotation was present prior to this DRC, and the DRC did not appear to significantly alter the low-level horizontal wind field (Fig. 18), in contrast to the majority of the DRCs studied by Rasmussen et al. (2006) and Kennedy et al. (2007a). Again, it is possible that the dynamical importance of the DRC in the simulation may have been diminished by the presence of an unrealistically strong cold pool.

Both the type I and type II DRCs originate at somewhat lower altitudes in the simulation than in observed supercells for which radar data extend to the storm summit (e.g., Fig. 3). The autoconversion scheme used in the Kessler (1969) microphysics parameterization biases rainwater production to relatively low altitudes and this may have contributed to the formation of DRCs at unrealistically low elevations in the simulation.

3) DRC FORMATION RESULTING FROM THE INTENSIFICATION OF LOW-LEVEL ROTATION (TYPE III)

A third type of DRC was observed in the simulation at times when a hook echo and strong near-surface vortex were already present. Figures 20 and 21 show the evolution of one such DRC from 11 520 to 12 120 s. It is evident that a protuberance in the rainwater isosurface descends toward the ground during this time period, enhancing the ''ball'' at the end of the hook echo. Horizontal cross sections of rainwater mixing ratio near the surface (not shown) suggest a maximum that significantly exceeds the minimum along the path from the DRC to the main cell echo region, satisfying the Rasmussen et al. (2006) DRC criterion. This type of DRC was smaller in horizontal extent compared to the other two types (~500 m versus ~1 km). Like the type II DRCs observed during supercell cycling, it did not significantly alter the low-level horizontal wind field.

This type of DRC arises as a result of the amplification of near-surface vorticity and an attendant reversal of the dynamic vertical pressure gradient force (we define this as a type III DRC; Fig. 22). This is the same mechanism by which occlusion downdrafts are observed to develop in supercell thunderstorms (Klemp and Rotunno 1983). As the near-surface vorticity increases, a downdraft intensifies near the axis of rotation, thereby allowing hydrometeors to descend toward the ground within a narrow column as a DRC. At 11 520 s, vertical vorticity is a maximum ($\sim 0.30\ s^{-1}$) at the lowest model level and rapidly decreases with height (Fig. 21a). The vortex is collocated with a strong axial downdraft ($w < -5\ m\ s^{-1}$) that extends to ap-

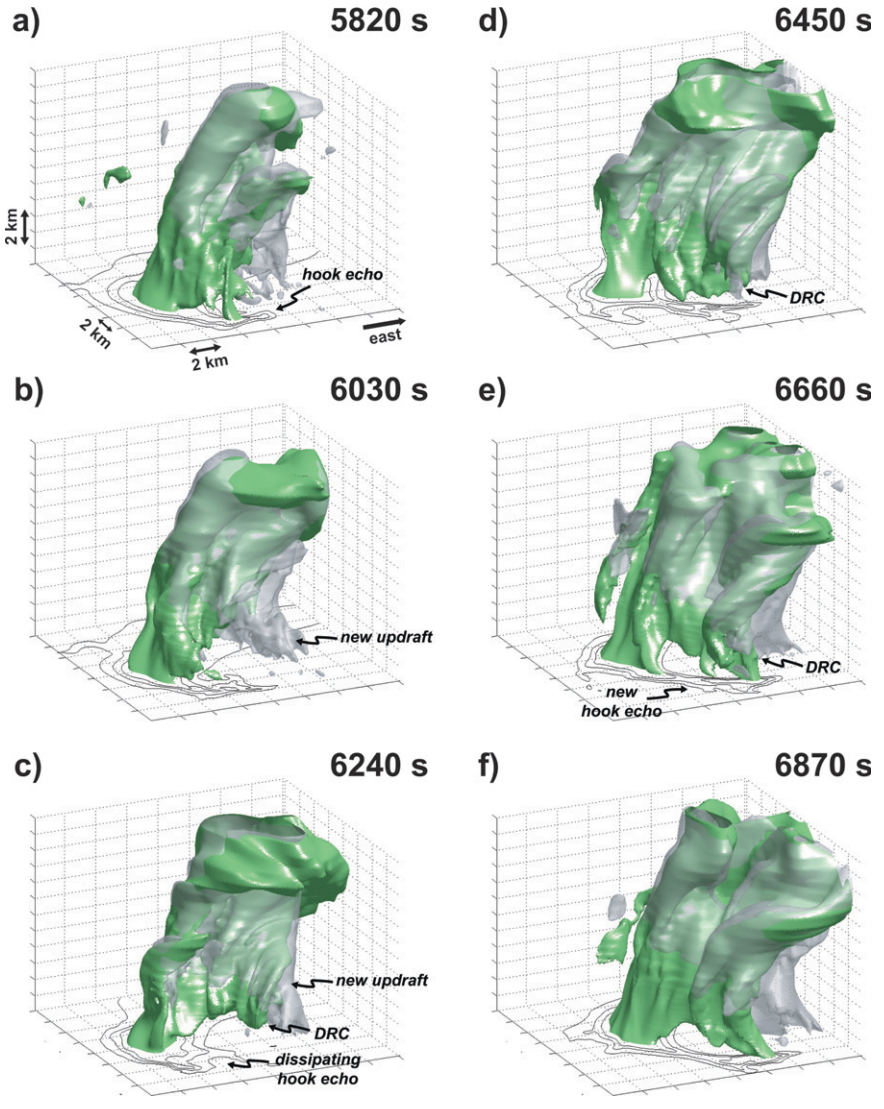

FIG. 17. (a)–(f) Evolution of the 4.0 g kg^{-1} rainwater mixing ratio (green) and 12 m s^{-1} vertical velocity (gray) isosurfaces in the three-dimensional numerical simulation from (a)–(f) 5820 to 6870 s. The 1, 2, and 3 g kg^{-1} rainwater mixing ratio contours at $z = 35$ m (the lowest model level) also are plotted. The view is from the southwest.

proximately 1500 m, allowing rainwater to fall to the surface as a DRC. By 11 880 s, the 2.5 g kg^{-1} rainwater isosurface reaches the surface within the vortex (Fig. 20d).

4. Summary and closing remarks

Observations of DRCs by mobile Doppler radar (the DOW radars) have been documented herein. In some cases the DRCs eluded detection by the WSR-88D, presumably owing to large distances between the parent storm and the WSR-88D. In one case (27 May 1997), a snapshot of reflectivity isosurfaces suggested the presence of a DRC, but the descent of the region of enhanced reflectivity could not be established in an examination of the time evolution of the reflectivity isosurfaces. Although the low-level radial velocity field occasionally underwent significant changes (e.g., increased rear-to-front flow and an increase in azimuthal wind shear) following the arrival of the DRC at low levels (e.g., 29 May 2001a), as has been found in past studies, the dynamical connection between the DRC and the changes in the wind field was difficult to establish given the considerable temporal and spatial separation between the DRC and the wind accelerations (as in the 29 May 2001a case). In other cases, DRCs were not accompanied by significant increases in the low-

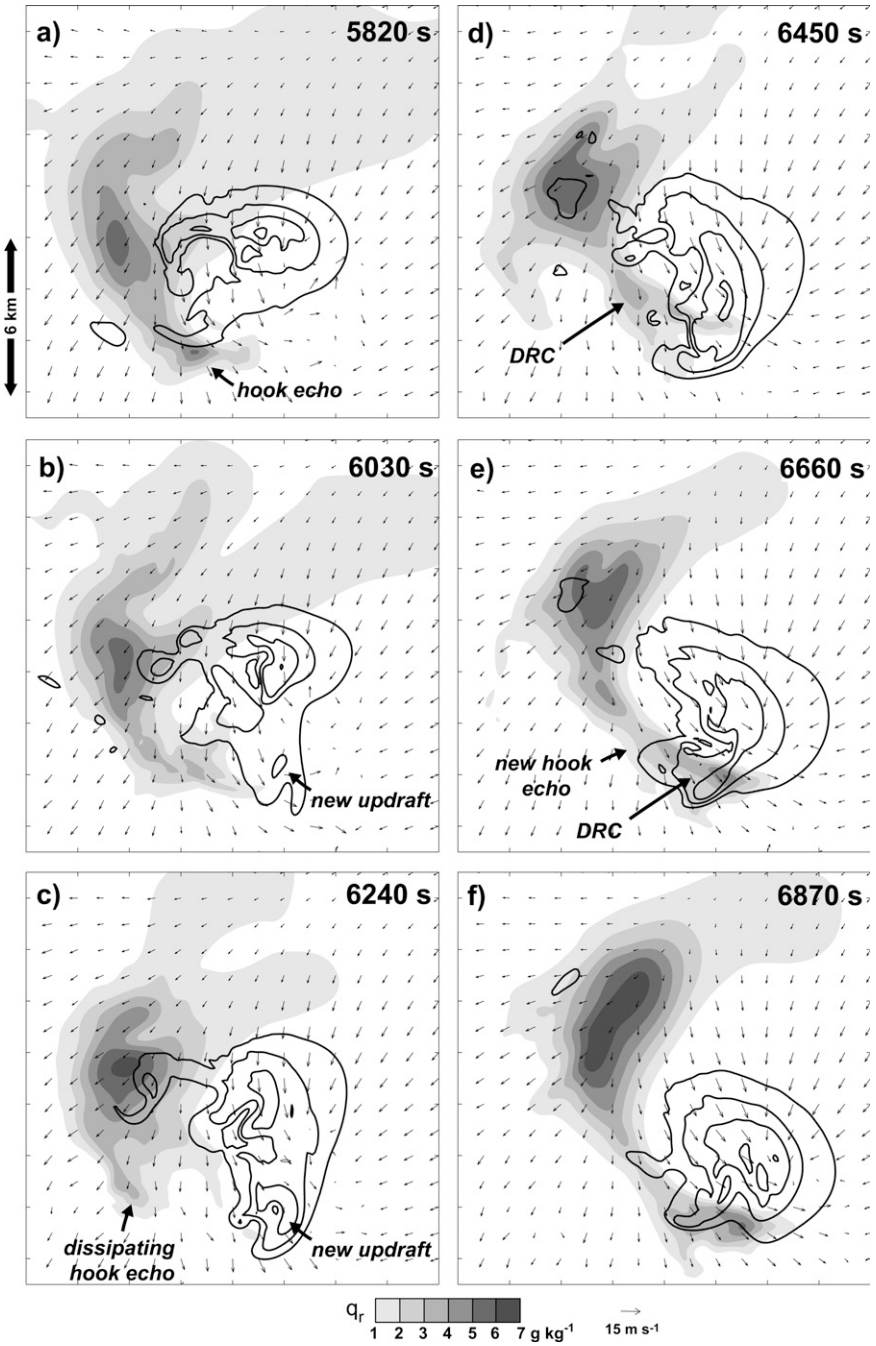

FIG. 18. Rainwater mixing ratio (q_r) at 35 m (the lowest model level; gray shading—see legend), vertical velocity (black contours of 7, 14, 21, and 28 m s^{-1}) at 3.5 km, and horizontal velocity vectors (see legend; vectors are plotted at every tenth grid point) at 35 m at (a) 5820, (b) 6030, (c) 6240, (d) 6450, (e) 6660, and (f) 6870 s, respectively. The domain is identical to that shown in Fig. 17.

level rear-to-front flow (e.g., 29 May 2001b, 5 June 2001) or azimuthal wind shear (e.g., 29 May 2001b). Thus, we are unable to generalize relationships between DRCs and changes in the low-level wind field.

Numerous DRCs were observed in a three-dimensional numerical simulation of a supercell thunderstorm. The DRCs were classified as follows: (i) those forming as a result of midlevel flow ''stagnation'' (type I); (ii) those resulting from precipitation that forms within a new updraft that eventually merges with the

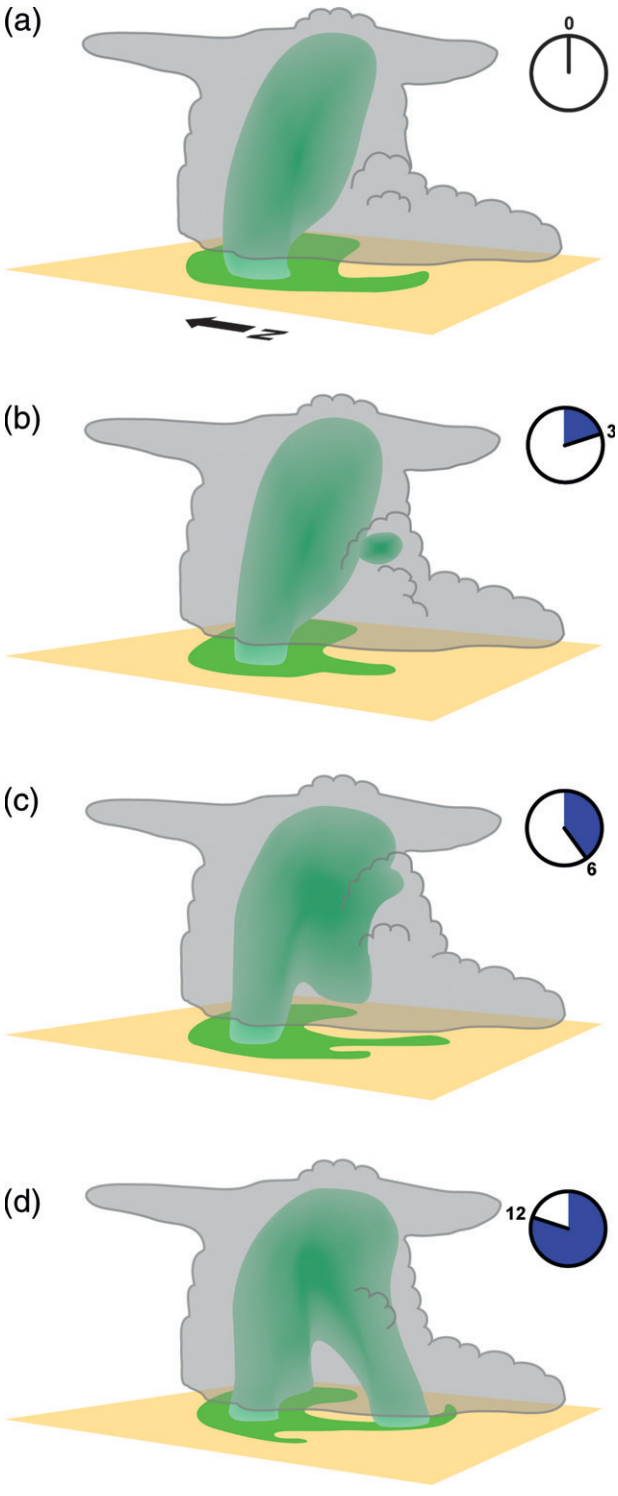

main updraft, such as the process that occurs in conjunction with updraft–mesocyclone "cycling" (type II); and (iii) those that descended down the axis of an amplifying low-level vertical vorticity maximum (type III). It is not likely that such classifications can be made using single-Doppler radar data alone in an operational setting. Of the three types of DRCs, type I DRCs seem the most likely to be associated with dynamical processes that can lead to a subsequent rapid increase in low-level rotation, such as that documented by Rasmussen et al. (2006) and Kennedy et al. (2007a), although even for the type I DRC identified in the numerical simulation, it does not seem likely that the DRC contributed in a direct way to the outflow surge that preceded the rapid intensification of a vortex (e.g., Fig. 13), as has been proposed by Rasmussen et al. (2006) and Kennedy et al. (2007a). In the case of type II DRCs, low-level rotation tended to increase in the 5–15-min period after the DRC reached the surface, but this trend was a regular part of the cyclic behavior of the simulated supercell and does not appear to be tied directly to these DRCs; that is, all new updraft–mesocyclone cycles were characterized by an increase in low-level rotation independent of whether the formation of the new hook echo involved a DRC. In the case of type III DRCs, DRC formation was a by-product of the amplification of low-level rotation, rather than a precursor of low-level rotation amplification. In summary, a straightforward relationship between DRCs and changes in the low-level wind field was not found in the mobile radar observations or in the numerical simulation. Regarding this relationship in the numerical simulation, we reiterate the caveat that the Kessler microphysics scheme tends to lead to unrealistically cold outflow, and it is possible that the dynamical effects of a DRC would be diminished in such a simulation. Then again, even in the DOW-observed DRC cases, we did not find that DRCs are systematically accompanied by an intensification of low-level rotation.

The DRCs in the numerical simulation were similar in appearance to the DRCs observed in the mobile ra-

←

FIG. 19. Conceptual model of a type II DRC. The cloud outline is gray, the dark green isosurface represents larger rainwater concentrations (nominally $q_r > 3$ g kg^{-1}), and the rainwater field ($q_r > 0$ g kg^{-1}) at the surface is shaded light green. The procession of time is illustrated by the clocks (numerals indicate minutes past the initial time). The evolution is as follows: (a) a new updraft on the southern flank (right flank, looking downshear) grows; (b) rainwater is generated at the summit of the new updraft (it may merge with the main region of hydrometeors associated with the primary updraft); (c) the new rain falls down the western flank of the new updraft as a DRC, resulting in a new hook echo at low levels east (downshear) of the original hook echo, which dissipates; and (d) the new updraft that had been initiated on the right flank of the primary updraft now becomes the new primary updraft.

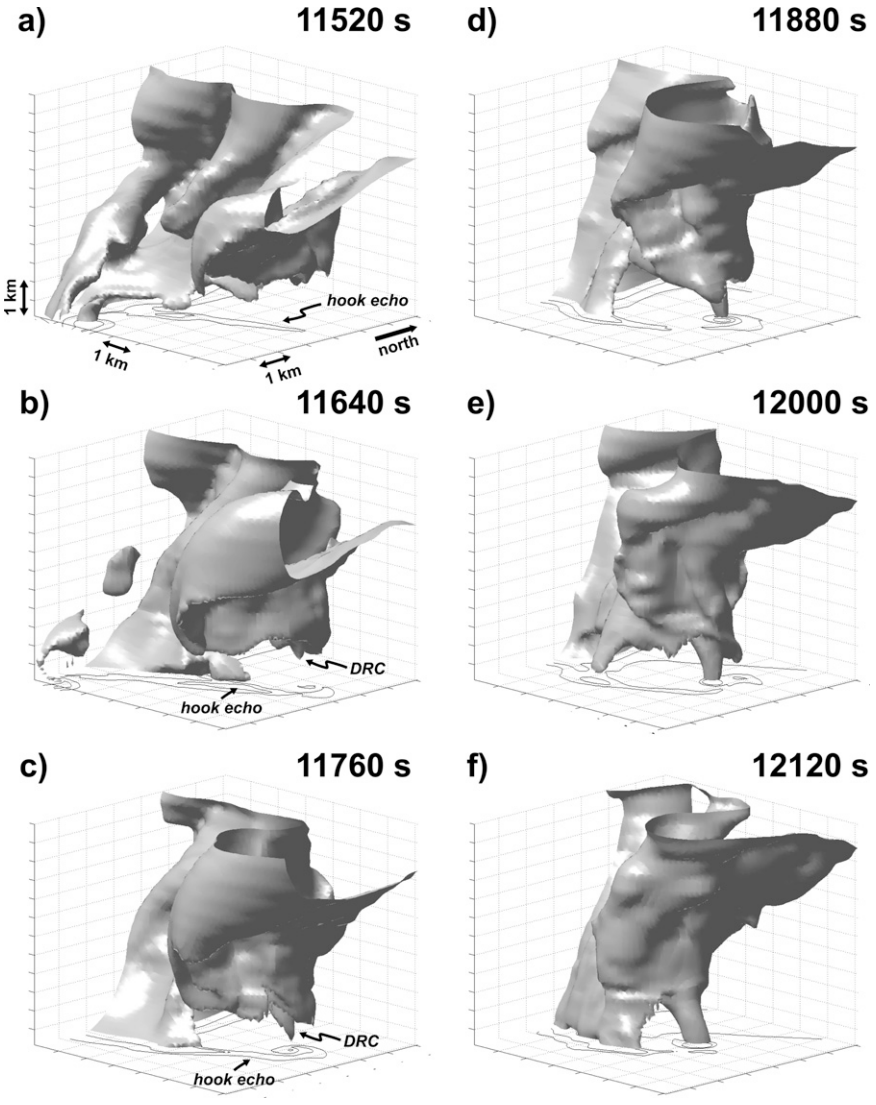

FIG. 20. (a)–(f) Evolution of the 2.5 g kg^{-1} rainwater mixing ratio isosurface in the three-dimensional numerical simulation from 11 520 to 12 120 s. The 1 and 2 g kg^{-1} rainwater mixing ratio contours at z = 35 m (the lowest model level) also are plotted. The view is from the southeast.

dar data and in past WSR-88D studies. Of the DRCs observed by the DOWs in this study, we tentatively identify the DRC in the 5 June 2001 case as a type II DRC. The 29 May 2001a case, as discussed in section 2, has similarities with the case documented by Lemon (1976) whereby the hook echo formed following the merger of a flanking-line updraft with the main storm. Thus, the 29 May 2001a case might be another example of what is essentially a type II DRC in that the precipitation responsible for the DRC formed within a growing updraft initially separated from the main updraft. We are less certain of the formation mechanisms in the 29 May 2001b and 26 May 2000 cases, but the limited evidence suggests that type I might be most likely (in the 29 May 2001b case, recall that there also were questions about the relationship between the outflow surge and the DRC, just as was the case for the type I DRC seen in the numerical simulation). None of the five DOW-observed DRC events presented herein appear to be examples of type III DRCs, although it is believed that such DRCs might have been observed in the past by the DOWs in conjunction with DOW tornadogenesis observations; these observations may be presented in a future article.

The fact that several mechanisms were identified by which DRCs developed in the model, only one of which

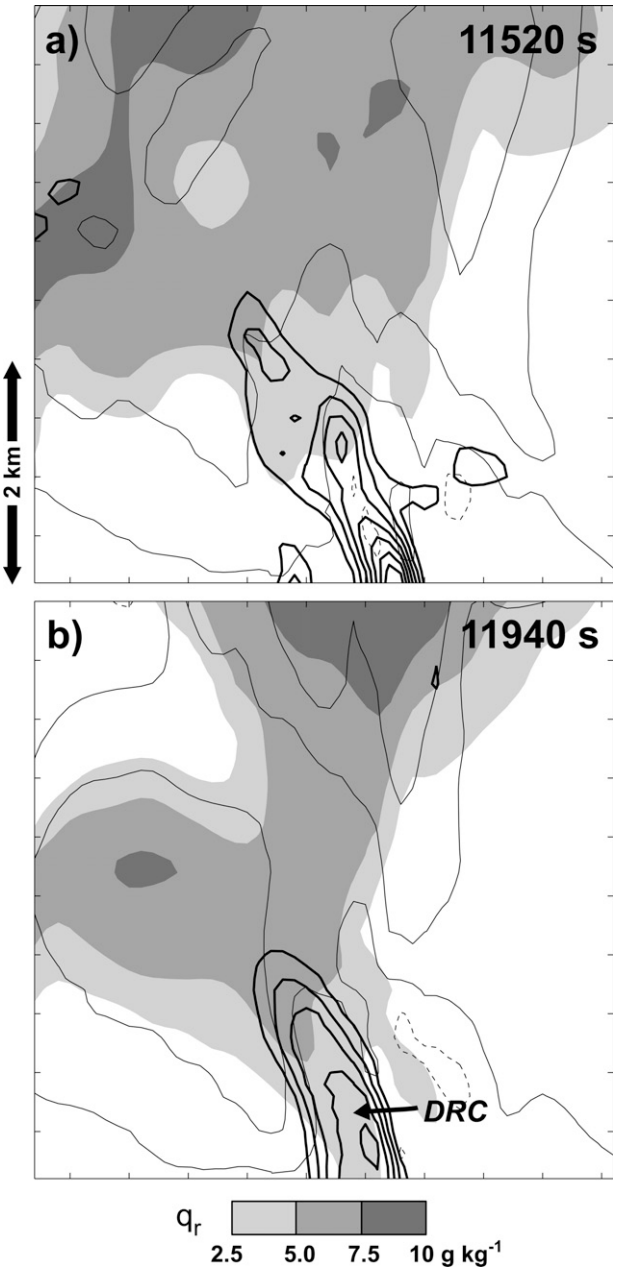

FIG. 21. West–east-oriented vertical cross sections through the center of the DRC (a) just prior to DRC occurrence (11 520 s) and (b) after the DRC has reached the surface (11 940 s). The cross sections show rainwater mixing ratio (shaded; see legend), vertical velocity (thin black contours; 10 m s^{-1} interval from −5 to 25 m s^{-1}; negative contours are dashed), and vertical vorticity (heavy solid contours beginning at 0.04 s^{-1} and contoured at an interval of 0.04 s^{-1}).

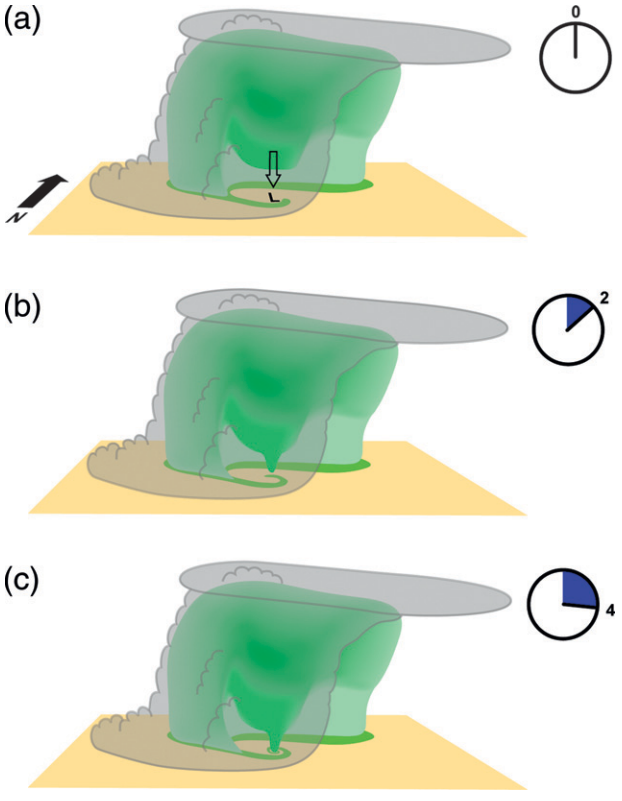

FIG. 22. Conceptual model of a type III DRC. The cloud outline is gray, the dark green isosurface represents larger rainwater concentrations (nominally $q_r > 3$ g kg^{-1}), the rainwater field ($q_r > 0$ g kg^{-1}) at the surface is shaded light green, and the presence of a dynamic pressure minimum and direction of the attendant dynamic vertical pressure gradient are indicated with an "L" and open arrow, respectively. The procession of time is illustrated by the clocks (numerals indicate minutes past the initial time). The evolution is as follows: (a)→(b) rotation increases at low levels to an extent such that the low-level rotation exceeds the midlevel rotation, resulting in a downward-directed dynamic vertical pressure gradient force, and (c) the reversal of the vertical pressure gradient leads to a weakening of the updraft along the axis of rotation, thereby allowing previously suspended rainwater to descend toward the ground as a DRC.

was closely followed by rapid low-level vorticity intensification, might account for the fact that prior DRC studies (e.g., Kennedy et al. 2007a) have produced somewhat mixed results with respect to the potential of DRC detection to aid in forecasting low-level rotation intensification and subsequent tornadogenesis. It is not possible to say what mechanism(s) led to the DRCs in each of the cases observed by Rasmussen et al. (2006) and Kennedy et al. (2007a).

Given that the DOWs observe many DRCs that the WSR-88D fails to detect, and that DRCs are common in numerical simulations of supercells (as a result of our heightened awareness, we have found them in many more simulations than the simulation presented in section 3), DRCs may be much more common in supercells than prior studies have found. One might wonder whether the likely underdetection of DRCs has exaggerated the connection between DRCs and subsequent increases in low-level rotation suggested by previous

work.[3] Future work might consider an investigation of the dynamical cause-and-effect relationship between DRCs and the development or intensification of low-level rotation, with an emphasis on the case of the type I DRC that developed within the numerical simulation between 3420 and 3780 s and the genesis of the intense vorticity maximum shortly thereafter. Another obvious topic to consider exploring in the future is DRC formation in a larger numerical simulation parameter space, whereby a range of microphysics parameterizations are employed.

Acknowledgments. We are grateful to the volunteers who tirelessly collected data in support of the DOW field activities. We thank Erik Rasmussen, Jerry Straka, and Aaron Kennedy for motivating this study and sharing their thoughts on supercell rear-flank precipitation processes, and Johannes Verlinde for reviewing an earlier version of this work as a member of the lead author's M.S. committee. We also thank Jeff Beck for providing edited radar data from the 29 May 2001 case. Careful reviews provided by three anonymous reviewers are greatly appreciated as well. Support from NSF Grant ATM-0437512 also is acknowledged, as is support for the lead author by way of an American Meteorological Society Graduate Fellowship, which was sponsored by NASA's Earth Science Enterprise.

REFERENCES

Adlerman, E. J., 2003: Numerical simulations of cyclic storm behavior: Mesocyclogenesis and tornadogenesis. Ph.D. dissertation, University of Oklahoma, 226 pp. [Available from School of Meteorology, University of Oklahoma, 120 David L. Boren Blvd., Ste. 5900, Norman, OK 73072.]

——, K. K. Droegemeier, and R. P. Davies-Jones, 1999: A numerical simulation of cyclic mesocyclogenesis. *J. Atmos. Sci.,* **56,** 2045–2069.

Agee, E. M., J. T. Snow, and P. Clare, 1976: Multiple vortex features in the tornado cyclone and the occurrence of tornado families. *Mon. Wea. Rev.,* **104,** 552–563.

Arnott, N., Y. Richardson, J. Wurman, and E. N. Rasmussen, 2006: Relationship between a weakening cold front, misocyclones, and cloud development on 10 June 2002 during IHOP. *Mon. Wea. Rev.,* **134,** 311–335.

Barnes, S. L., 1964: A technique for maximizing details in numerical weather map analysis. *J. Appl. Meteor.,* **3,** 396–409.

Bluestein, H. B., and S. G. Gaddy, 2001: Airborne pseudo-dual-Doppler analysis of a rear-inflow jet and deep convergence zone within a supercell. *Mon. Wea. Rev.,* **129,** 2270–2289.

Browning, K. A., 1964: Airflow and precipitation trajectories within severe local storms which travel to the right of the winds. *J. Atmos. Sci.,* **21,** 634–639.

——, 1965: The evolution of tornadic storms. *J. Atmos. Sci.,* **22,** 664–668.

Burgess, D. W., V. T. Wood, and R. A. Brown, 1982: Mesocyclone evolution statistics. Preprints, *12th Conf. on Severe Local Storms*, San Antonio, TX, Amer. Meteor. Soc., 422–424.

Chisholm, A. J., 1973: Alberta hailstorms. Part I: Radar case studies and airflow models. *Alberta Hailstorms, Meteor. Monogr.,* No. 36, Amer. Meteor. Soc., 1–36.

Darkow, G. L., and J. C. Roos, 1970: Multiple tornado producing thunderstorms and their apparent cyclic variations in intensity. Preprints, *14th Conf. on Radar Meteorology,* Tucson, AZ, Amer. Meteor. Soc., 305–308.

Emanuel, K. A., 1994: *Atmospheric Convection.* Oxford University Press, 580 pp.

Forbes, G. S., 1975: Relationship between tornadoes and hook echoes associated with left-turn tornado families. Preprints, *Ninth Conf. on Severe Local Storms,* Norman, OK, Amer. Meteor. Soc., 280–285.

——, 1977: Thunderstorm-scale variations of echoes associated with left-turn tornado families. Preprints, *10th Conf. on Severe Local Storms,* Omaha, NE, Amer. Meteor. Soc., 321–326.

——, 1981: On the reliability of hook echoes as tornado indicators. *Mon. Wea. Rev.,* **109,** 1457–1466.

Fujita, T. T., 1958: Mesoanalysis of the Illinois tornadoes of 9 April 1953. *J. Meteor.,* **15,** 288–296.

——, 1965: Formation and steering mechanisms of tornado cyclones and associated hook echoes. *Mon. Wea. Rev.,* **93,** 67–78.

——, 1975: New evidence from April 3–4, 1974 tornadoes. Preprints, *Ninth Conf. on Severe Local Storms,* Norman, OK, Amer. Meteor. Soc., 248–255.

——, D. L. Bradbury, and C. F. Van Thullenar, 1970: Palm Sunday tornadoes of April 11, 1965. *Mon. Wea. Rev.,* **98,** 29–69.

Garrett, R. A., and V. D. Rockney, 1962: Tornadoes in northeastern Kansas, May 19, 1960. *Mon. Wea. Rev.,* **90,** 231–240.

Jensen, B., T. P. Marshall, M. A. Mabey, and E. N. Rasmussen, 1983: Storm scale structure of the Pampa storm. Preprints, *13th Conf. on Severe Local Storms,* Tulsa, OK, Amer. Meteor. Soc., 85–88.

Johnson, K. W., P. S. Ray, B. C. Johnson, and R. P. Davies-Jones, 1987: Observations related to the rotational dynamics of the 20 May 1977 tornadic storms. *Mon. Wea. Rev.,* **115,** 2463–2478.

Kennedy, A. D., J. M. Straka, and E. N. Rasmussen, 2007a: A statistical study of the association of DRCs with supercells and tornadoes. *Wea. Forecasting,* **22,** 1192–1199.

——, ——, and ——, 2007b: A visual observation of the 6 June 2005 descending reflectivity core. *Electron. J. Severe Storms Meteor.,* **2** (6). [Available online at http://www.ejssm.org/ojs/index.php/ejssm/article/viewArticle/16/28.]

Kessler, E., 1969: *On the Distribution and Continuity of Water Substance in Atmospheric Circulations. Meteor. Monogr.,* No. 10, Amer. Meteor. Soc., 84 pp.

Klemp, J. B., and R. Rotunno, 1983: A study of the tornadic region within a supercell thunterstorm. *J. Atmos. Sci.,* **40,** 359–377.

Lemon, L. R., 1976: The flanking line, a severe thunderstorm intensification source. *J. Atmos. Sci.,* **33,** 686–694.

[3] Similarly, one could argue that the underdetection of mesocyclones prior to the nationwide installation of a Doppler radar network in the mid-1990s contributed to unrealistically high expectations for warning improvements based on mesocyclone detection. As more and more mesocyclones were detected following the widespread availability of Doppler radar data, the percentage of mesocyclones known to be tornadic declined (Trapp et al. 2005), as did the expected skill of tornado warnings based on mesocyclone detections alone.

——, 1977: Severe thunderstorm evolution: Its use in a new technique for radar warnings. Preprints, *10th Conf. on Severe Local Storms,* Omaha, NE, Amer. Meteor. Soc., 77–83.

——, 1982: New severe thunderstorm radar identification techniques and warning criteria: A preliminary report. NOAA Tech. Memo. NWS NSSFC-1, 60 pp. [NTIS PB-273049.]

——, and C. A. Doswell III, 1979: Severe thunderstorm evolution and mesocyclone structure as related to tornadogenesis. *Mon. Wea. Rev.*, **107,** 1184–1197.

Markowski, P. M., 2002: Hook echoes and rear-flank downdrafts: A review. *Mon. Wea. Rev.,* **130,** 852–876.

——, 2008: A comparison of the midlevel kinematic characteristics of a pair of supercell thunderstorms observed by airborne Doppler radar. *Atmos. Res.,* **88,** 314–322, doi:10.1016/j.atmosres.2007.11.026.

——, J. M. Straka, and E. N. Rasmussen, 2002: Direct surface thermodynamic observations within the rear-flank downdrafts of nontornadic and tornadic supercells. *Mon. Wea. Rev.,* **130,** 1692–1721.

——, C. Hannon, and E. Rasmussen, 2006: Observations of convection initiation ''failure'' from the 12 June 2002 IHOP deployment. *Mon. Wea. Rev.,* **134,** 375–405.

Marwitz, J. D., 1972: The structure and motion of severe hailstorms. Part I: Supercell storms. *J. Appl. Meteor.,* **11,** 166–179.

Pauley, P. M., and X. Wu, 1990: The theoretical, discrete, and actual response of the Barnes objective analysis scheme for one- and two-dimensional fields. *Mon. Wea. Rev.,* **118,** 1145–1163.

Rasmussen, E. N., J. M. Straka, M. S. Gilmore, and R. Davies-Jones, 2006: A preliminary survey of rear-flank descending reflectivity cores in supercell storms. *Wea. Forecasting,* **21,** 923–938.

Ray, P. S., B. C. Johnson, K. W. Johnson, J. S. Bradberry, J. J. Stephens, K. K. Wagner, R. B. Wilhelmson, and J. B. Klemp, 1981: The morphology of several tornadic storms on 20 May 1977. *J. Atmos. Sci.,* **38,** 1643–1663.

Skamarock, W. C., and J. B. Klemp, 1993: Adaptive grid refinement for 2D and 3D nonhydrostatic atmospheric flow. *Mon. Wea. Rev.,* **121,** 788–804.

Snow, J. T., and E. M. Agee, 1975: Vortex splitting in the mesocyclone and the occurrence of tornado families. Preprints, *Ninth Conf. on Severe Local Storms,* Norman, OK, Amer. Meteor. Soc., 270–277.

Stout, G. E., and F. A. Huff, 1953: Radar records Illinois tornadogenesis. *Bull. Amer. Meteor. Soc.,* **34,** 281–284.

Straka, J. M., E. N. Rasmussen, R. P. Davies-Jones, and P. M. Markowski, 2007: An observational and idealized numerical examination of low-level counter-rotating vortices toward the rear flank of supercells. *Electron. J. Severe Storms Meteor.,* **2** (8). [Available online at http://www.ejssm.org/ojs/index.php/ejssm/article/view/32.]

Trapp, R. J., and C. A. Doswell III, 2000: Radar data objective analysis. *J. Atmos. Oceanic Technol.*, **17,** 105–120.

——, G. J. Stumpf, and K. L. Manross, 2005: A reassessment of the percentage of tornadic mesocyclones. *Wea. Forecasting,* **20,** 680–687.

Wurman, J., 2001: The DOW mobile multiple Doppler network. Preprints, *30th Int. Conf. on Radar Meteorology,* Munich, Germany, Amer. Meteor. Soc., 95–97. [Available online at http://ams.confex.com/ams/pdfpapers/21572.pdf.]

——, J. Straka, E. Rasmussen, M. Randall, and A. Zahrai, 1997: Design and deployment of a portable, pencil-beam, pulsed, 3-cm Doppler radar. *J. Atmos. Oceanic Technol.,* **14,** 1502–1512.

——, Y. Richardson, C. Alexander, S. Weygandt, and P. F. Zhang, 2007: Dual-Doppler and single-Doppler analysis of a tornadic storm undergoing mergers and repeated tornadogenesis. *Mon. Wea. Rev.,* **135,** 736–758.

Xue, M., K. K. Drogemeier, and V. Wong, 2000: The Advanced Regional Prediction System (ARPS)—A multiscale nonhydrostatic atmospheric simulation and prediction tool. Part I: Model dynamics and verification. *Meteor. Atmos. Phys.,* **75,** 161–193.

——, and Coauthors, 2001: The Advanced Regional Prediction System (ARPS)—A multiscale nonhydrostatic atmospheric simulation and prediction tool. Part II: Model physics and applications. *Meteor. Atmos. Phys.*, **76,** 143–165.

——, D. H. Wang, J. D. Gao, K. Brewster, and K. K. Drogemeier, 2003: The Advanced Regional Prediction System (ARPS), storm-scale numerical weather prediction and data assimilation. *Meteor. Atmos. Phys.,* **82,** 139–170.